NANOSCALE LIGHT CONFINEMENT: PRINCIPLES, MEASUREMENT, AND APPLICATIONS

A Dissertation

Presented to the Faculty of the Graduate School

of Cornell University

in Partial Fulfillment of the Requirements for the Degree of

Doctor of Philosophy

by

Jacob Thomas Robinson

January 2009

NANOSCALE LIGHT CONFINEMENT:

PRINCIPLES, MEASUREMENT, AND APPLICATIONS

Jacob Thomas Robinson, Ph.D.

Cornell University 2009

By confining photons to small volumes for long periods of time, optical nanocavities offer the ability to greatly enhance the interaction between light and matter. This can greatly improve the efficiency of photonic devices as well as lead to novel physical phenomena. While over the past several years resonators have improved to confine photons for longer periods of time, the volume in which light can be confined has remained relatively stagnant on the order of a cubic half-wavelength which has been thought to be the fundamental limit.

In this dissertation we demonstrate that the effective mode volume of optical resonant cavities can be reduced below a cubic half-wavelength. We develop novel tools to characterize these highly confined optical modes, and utilize this light confinement to achieve efficient light-matter interaction in photonic devices. Finally we present novel physical phenomena which result from this nanoscale light confinement.

The dissertation is organized into six chapters. Chapter 1 gives a brief introduction to photonics and the reasons for pursuing nanoscale light confinement. In Chapter 2 we define the effective mode volume and discuss its theoretical limit. We show with analytical and numerical calculations that contrary to previous assumptions sub-wavelength-sized dielectric structures can enable mode volumes smaller than a cubic half-wavelength. In Chapter 3 we dis-

cuss experimental techniques for measuring these ultra-small mode volumes. We introduce a new high-resolution near field measurement technique called Transmission-based Near-field Scanning Optical Microscopy (TraNSOM), and show experimental results verifying nanoscale light confinement in our devices. In Chapter 4 we discuss applications for these small-mode-volume devices. We show analytically and numerically that these devices can be surprisingly efficient for achieving gain and lasing in an electrically-pumped silicon-based platform, and we experimentally demonstrate highly sensitive detection of acetylene gas. In Chapter 5 we discuss new physical phenomena associated with small volume optical resonant cavities. We show that these cavities can behave as an individual radiating dipole and, using the TraNSOM technique, the lifetime of this dipole can be modified at long distances. Chapter 6 gives a brief conclusion and outlook on the future of this field.

BIOGRAPHICAL SKETCH

Upstate New York. Somewhere between Binghamton and Slaterville. Jacob Robinson raced down route 79 in his '96 Suzuki Sidekick, Ernesto. His speedometer topped 85. 30-over is a felony in New York, but that didn't matter. Obeying the law is a luxury for those who aren't carrying the survival of the human race in the back seat of their car.

"This is not the way it's supposed to be Ernie," he said aloud. "What does a physicist know about espionage?" But Jacob Robinson was no ordinary physicist. The course of events, each one seemingly unremarkable, had prepared Jacob for this very day. The day that the fate of the world lay in a black case nestled between a red North Face backpack and Thursday's edition of the Cornell Daily Sun. He sighed and with the tranquil hills of central New York comprising a green blur out the car windows, he allowed his mind to wander backwards down the path that brought him to this day

The story began one joyful day in 1982 in Ventura, California. A relatively routine birth, Jacob's early life showed no signs of the danger and intrigue that would later envelope it. After completing high school in 1999 Jacob attended the University of California, Los Angeles where he earned a B.S. in Physics in 2003. In 2008 he completed his doctoral work at Cornell University and will commence post-doctoral studies at Harvard University in August with Hongkun Park's Research Group.

Yes, Jacob Robinson's future is very bright indeed...that is, if there is a future to speak of. As Jacob zoomed down the freeway, a casual observer would never imagine that standing between life as we know it and humanity's firey doom was nothing but a lightweight sports utility vehicle, a black briefcase, and one man. That man is Jacob Robinson. Dr. Robinson. And today, with Ernesto

purring steadily along, the future looks a little brighter and a lot less firey for everyone.

For my family: Jeff, Becky, Josh, Ellen & Ron.

ACKNOWLEDGEMENTS

There are countless people who have contributed directly or indirectly to the completion of this dissertation. I would like to devote this section to thank them for their help and support. While in many ways this is the most important section of this dissertation, it is also probably the least complete. There is simply not enough room and I am not a well enough equipped writer to adequately acknowledge all the people who deserve credit for their efforts. I apologize in advance for the brevity of these acknowledgements and to anyone whose name has been left out.

First and foremost I would like to thank my advisor Prof. Michal Lipson. Her support and mentorship over my formative years as a young scientist has had profoundly positive influence on me. I cannot overemphasize how much I value all I have learned from her and the positive academic environment she has fostered in her group. The majority of what I have learned from Prof. Lipson which I consider most important is not contained in the contents of this document (at least not at face value). By example Prof. Lipson has demonstrated how to become a successful scientist and assemble and advise an inspired and productive group. Through our discussions, editing of manuscripts, and preparations for presentations she has taught me how to think about problems, find solutions, and communicate my ideas to others. It is this skill set that she has helped me to develop which I consider to be the most valuable consequence of my dissertation work. Any future academic success that I might achieve is truly a credit to the training and mentorship she has provided.

In addition, I am enormously grateful for how hard Prof. Lipson has worked to promote the work of the group and equip the laboratories. Thanks to her tireless traveling and fund raising there has been scarcely a time when I've needed

something in the lab which could not be purchased immediately. Nor has there been a time when traveling outside of Cornell that I have received anything but the warmest welcome from people acquainted with Prof. Lipson and familiar with our work. This has made my life as a graduate student relatively easy.

Finally, Prof. Lipson has been an extremely nurturing advisor, concerned for each of her students not just as researchers but also as people. In this way she has assembled a group of talented students and postdocs and fostered among them a supportive and friendly environment. Because of this my time at Cornell has not only been productive but also enjoyable. Again I cannot express how much I have enjoyed and valued working for Prof. Lipson and in many ways I am saddened to be leaving.

I would also like to thank the other members of my special committee: Prof. Alexander L. Gaeta and Prof. Clifford R. Pollock. Their comments on this dissertation and discussions were critical in preparing it in its final form. In addition, I would like to thank Prof. Gaeta for his open collaboration. He and his group have been extremely approachable and amenable to sharing ideas, technical knowhow, and equipment which has been critical to executing a number of experiments. In particular the work with Acetylene gas in Chapter 4 was inspired heavily by conversations with Prof. Gaeta, and Dr. Aron Slepkov, Dr. Pablo Londero, and Amar Bhagwat from his group.

Other collaborators whom I would like to acknowledge include Prof. Oskar Painter at CalTech and Prof. Thomas Koch from Lehigh University who helped with the formulation of Section 4.2. Prof. Christopher "Kit" Umbach and Dr. Leon "Neon" Bellan provided probes and useful discussions regarding the scanned probe measurements in Chapter 3. Prof. Shanhui Fan at Stanford University provided useful discussions regarding Chapter 2.

I also want to acknowledge the mentors who first interested me in pursing science as a career. Prof. David Saltzberg at UCLA introduced me to the idea of majoring in physics and gave me my first job in a physics lab. Prof. Yahya Rahmat-Samii, also at UCLA, graciously accepted me into his lab as a freshman and with whom I published my first peer-reviewed journal paper. Prof. Hong-Wen Jiang, also at UCLA, gave me my first independent experiment and inspired me to pursue graduate studies in physics. I am indebted to each of them for the instrumental roles they played in helping me define my career choice.

This brings me to the surly bunch of folks I've been fortunate enough to share an office with for the last five years: the Cornell Nanophotonics Group members. Of course I would never admit as much to their face, but I am proud to have been able to work with such a fantastic group of people whom I consider both colleagues and friends. In addition to contributing general ideas and suggestions, help around the lab, and comments on papers and presentations, the group members have made my life here at Cornell enjoyable, and this is what I am most grateful for. I'll mention their names and a word or two in chronological order. The more elaborate stories and endorsements I will save for another occasion perhaps over a pint of beer in a less archival format. Vilson R. Almeida and Qianfan "The Destroyer" Xu were role models for me when I entered the group. In addition to being perhaps the most technically sound person I've work with, Qianfan was also known for his loquaciousness and Olympic caliber ping pong skills. Then there is "Papa" Carl B. Poitras who brings to the group a flair and fashion sense to rival my own, Bradley "Braddd" S. Schmidt who is my source for updates on Canadian political affairs, and "Preble" Stefan F. Preble. Dr. Christina Manolatou worked part time with our group for a couple years and her finite difference mode solver and finite difference

time domain code was used extensively in this dissertation. Then there is Amy "Amars" C. Turner-Foster and Mark "Markus" Foster. Mark joined the group by marriage and we are expecting them to produce new group members any time now. Linnell "Cubano" Martinez was with us shortly but had a big impact. Long "Dragon" Chen has been a joy to work with. He thoughtfully edited several of my papers and helped to fabricate the gas sensor used in Chapter 4. He has also helped me learn to speak Chinese. Alexander "Sashasmom" Gonderanko has also been great to work with. He is someone you can count on to be in the office at all hours. In fact he is sitting next to me right now as I type this at 5:30 am. Kyle "Big Red" Preston is a Cornell fan by birth and has also helped me edit papers and worked with me on Section 4.2. Sasikanth "Sasi" Manupatrini runs pretty much every club on campus and has been a great help in preparing papers and presentations. Arthur "Noonie" Nitkowski, won second place in the Cornell EDS ping pong tournament and never shies away from a friendly competition despite the fact that I nearly always beat him. Nicolas "Niki" Sherwood-Droz is the group's social director, three time winner of the Shirley Temple look-alike contest, and was an indispensable help while we were working in Brazil. Jake "#2" Levy is my advisor on all things basketball related. The promising group of new students and postdocs who continually ask important questions and challenge me to come up with reasonable sounding answers include: Jaime "El Mexicano" Cardenas, Muhammad "The Prophet" Adnan, Debo "G-bad" Olaosebikan, Bernardo "Bernie" Kyotoku, Gustavo "Gus" Wiederhecker. Last but not least I'd like to thank the magnanimous Kim Cotton who has kept our group organized and functioning for the last few years. I will miss working with all of you.

I would also like to thank some of the people who have provided the personal, emotional, and athletic support I've needed at times over the last five years. There are too many to list, but in particular I would like to thank my room mates, those who have kept me sane during late nights in the CNF, and those who have kept me sane in general: Leon "Neon" Bellan, Michael "Big Mike" Durst, Hamid "Carlton" Schricker, Elizabeth "New Mike" Strychalski, Richard "Rick" James Brown, Paul "Boy" George, Bojan "Rob" Ilic, Sabrina "PT" Steirwalt, Jessica "Jess" Griffith, Deborah "Debob" Press, and my family (Jeff, Becky, Josh, Ellen, and Ron) to whom this dissertation is dedicated.

Finally I would like thank the agencies whose funding and facilities supported this work including the National Science Foundation Center on Materials and Devices for Information Technology Research (CMDITR), DMR-0120967, the Cornell Center for Material Research, the National Science Foundation's CAREER Grant No. 0446571, the Air Force Office of Scientific Research under grant AFOSR F49620-03-1-0424, and the U.S. Air Force MURI program on "Electrically-Pumped Silicon-Based Lasers for Chip-Scale Nanophotonic Systems" supervised by Dr. Gernot Pomrenke. This work was performed in part at the Cornell NanoScale Facility, a member of the National Nanotechnology Infrastructure Network, which is supported by the National Science Foundation (Grant ECS 03-35765) and we made use of STC shared experimental facilities supported by the National Science Foundation under Agreement No. ECS-9876771.

TABLE OF CONTENTS

LIST OF FIGURES

CHAPTER 1

INTRODUCTION

The need for faster and more efficient communication and information processing has grown steadily over the past several decades. Since 1974 the capacity-distance product for telecommunications has grown by a factor of 10 every 4 years [1] indicating an ever increasing demand to send more information longer distances. This increase in the capacity-distance product puts enormous demands on the number and size of nodes needed to sustain such a network. If this trend continues without improvements in the network hardware or architecture, in twenty years optical network nodes will consume 10,000 times more energy and space.

By creating smaller and more efficient optical devices it might be possible to accommodate the increasing demand on optical communication without consuming additional financial and natural resources. Over the past several decades advancements in micro and nano fabrication have allowed scientists and engineers to construct devices with feature sizes comparable to the wavelength of light. With this precise control over device geometry has come the ability to accurately manipulate the wavefunction of optical photons dramatically altering the way light behaves. This field of study, known as photonics, has produced a number of engineering and scientific breakthroughs over the past several years.

Because so many components for optical communication such as lasers[2, 3], light emitting diodes[4], sensors[5, 6, 7], detectors[8, 9, 10], and modulators[11, 12, 13, 14] rely on the efficient interaction between light and matter, a large subset of photonic breakthroughs have been focused on enhancing this inter-

action by confining photons in time and space. Additionally, more futuristic technologies such as optical quantum computing[15], and quantum information processing[16, 17, 18] also greatly benefit from stronger light-matter interactions.

Photons are typically confined in time and space using optical micro or nano cavities which can be characterized by their quality factor (Q) and effective mode volume (V_{eff}). The Q factor is related to how long on average photons remain trapped in the resonator and V_{eff} is related to the volume in which the photons are confined. Since interaction between light and matter increases by both confining photons in a smaller volumes and by confining them for longer periods of time, the figure of merit for increasing light-matter interaction is typically the ratio Q/V_{eff}[19]. Thus there is a large effort in the photonics community to produce large quality factor small volume resonant cavities. Over the past several years the quality factors of micron scale resonant cavities has grown steadily to values in excess of 10^6 [20, 21, 22], however the effective mode volumes of these cavities have hovered on the order of a cubic half-wavelength.

In this dissertation we demonstrate how V_{eff} can be decreased below a cubic-half wavelength, introduce new techniques for characterizing these devices, demonstrate the resulting enhanced interaction between light and matter, and discuss additional physical consequences of this nanoscale light confinement.

BIBLIOGRAPHY

[1] E. B. Desurvire, "Capacity Demand and Technology Challenges for Lightwave Systems in the Next Two Decades," J. Lightwave Technol. **24,** 4697–4710 (2006).

[2] Y. Yamamoto, S. Machida, and G. Bjrk, "Microcavity semiconductor laser with enhanced spontaneous emission," Phys. Rev. A **44,** 657 (1991).

[3] O. Painter, R. K. Lee, A. Scherer, A. Yariv, J. D. O'Brien, P. D. Dapkus, and I. Kim, "Two-dimensional photonic band-gap defect mode laser," Science **284,** 1819–21 (1999).

[4] C. Zinoni, B. Alloing, C. Paranthoen, and A. Fiore, "Three-dimensional wavelength-scale confinement in quantum dot microcavity light-emitting diodes," Appl. Phys. Lett. **85,** 2178–80 (2004).

[5] T. J. Kippenberg, S. M. Spillane, and K. J. Vahala, "Demonstration of ultra-high-Q small mode volume toroid microcavities on a chip," Appl. Phys. Lett. **85,** 6113–15 (2004).

[6] B. Schmidt, V. Almeida, C. Manolatou, S. Preble, and M. Lipson, "Nanocavity in a silicon waveguide for ultrasensitive nanoparticle detection," Appl. Phys. Lett. **85,** 4854–6 (2004).

[7] J. T. Robinson, L. Chen, and M. Lipson, "On-chip gas detection in silicon optical microcavities," Opt. Express **16,** 4296–4301 (2008).

[8] L. Chen, P. Dong, and M. Lipson, "High performance germanium photodetectors integrated on submicron silicon waveguides by low temperature wafer bonding," Optics Express **16,** 11513–11518 (2008).

[9] T. Yin, R. Cohen, M. M. Morse, G. Sarid, Y. Chetrit, D. Rubin, and M. J. Paniccia, "31 GHz Ge n-i-p waveguide photodetectors on Silicon-on-Insulator substrate," Optics Express **15,** 13965–13971 (2007).

[10] L. Vivien *et al.*, "High speed and high responsivity germanium photodetector integrated in a Silicon-On-Insulator microwaveguide," Optics Express **15,** 9843–9848 (2007).

[11] Q. Xu, B. Schmidt, S. Pradhan, and M. Lipson, "Micrometre-scale silicon electro-optic modulator," Nature **435,** 325–7 (2005).

[12] Y.-H. Kuo, Y. K. Lee, Y. Ge, S. Ren, J. E. Roth, T. I. Kamins, D. A. B. Miller, and J. S. Harris, "Strong quantum-confined Stark effect in germanium quantum-well structures on silicon," Nature **437,** 1334–1336 (2005).

[13] A. Liu, R. Jones, L. Liao, D. Samara-Rubio, D. Rubin, O. Cohen, R. Nicolaescu, and M. Paniccia, "A high-speed silicon optical modulator based on a metal-oxide-semiconductor capacitor," Nature **427,** 615–618 (2004).

[14] T. Baehr-Jones, M. Hochberg, W. Guangxi, R. Lawson, Y. Liao, P. A. Sullivan, L. Dalton, A. K. J. Jen, and A. Scherer, "Optical modulation and detection in slotted silicon waveguides," Opt. Express 13 (2005).

[15] M. Trupke, J. Goldwin, B. Darquie, G. Dutier, S. Eriksson, J. Ashmore, and E. A. Hinds, "Atom Detection and Photon Production in a Scalable, Open, Optical Microcavity," Phys. Rev. Lett. **99,** 063601–4 (2007).

[16] J. E. Sharping, K. F. Lee, M. A. Foster, A. C. Turner, B. S. Schmidt, M. Lipson, A. L. Gaeta, and P. Kumar, "Generation of correlated photons in nanoscale silicon waveguides," Optics Express **14,** 12388–12393 (2006).

[17] E. Burstein and C. Weisbuch, *Confined Electrons and Photons: New Physics and Applications*, 1 ed. (Springer, 1995), p. 918.

[18] A. Imamoglu, D. D. Awschalom, G. Burkard, D. P. DiVincenzo, D. Loss, M. Sherwin, and A. Small, "Quantum Information Processing Using Quantum Dot Spins and Cavity QED," Phys. Rev. Lett. **83,** 4204 (1999).

[19] K. J. Vahala, "Optical microcavities," Nature **424,** 839–846 (2003).

[20] D. K. Armani, T. J. Kippenberg, S. M. Spillane, and K. J. Vahala, "Ultra-high-Q toroid microcavity on a chip," Nature **421,** 925–928 (2003).

[21] B.-S. Song, S. Noda, T. Asano, and Y. Akahane, "Ultra-high-Q photonic double-heterostructure nanocavity," Nat Mater **4,** 207–210 (2005).

[22] E. Kuramochi, M. Notomi, S. Mitsugi, A. Shinya, T. Tanabe, and T. Watanabe, "Ultrahigh-Q photonic crystal nanocavities realized by the local width modulation of a line defect," Appl. Phys. Lett. **88,** 041112–3 (2006).

CHAPTER 2

BEATING THE "DIFFRACTION LIMIT" IN DIELECTRICS

2.1 Introduction

In transparent (dielectric) materials light is confined based on wave interference and therefore it is generally believed that the degree of confinement in each dimension is fundamentally limited to a half wavelength in the propagation medium ($\lambda/2n$ where n is the refractive index of the material [1, 2]). Since the efficiency of many photonic devices improves with increased light confinement [3, 4] considerable effort has been made to push below the $\lambda/2n$ limit (sometimes referred to as the diffraction limit [5, 6]). Surface plasmon polariton (SPP) modes confined to the surface of conducting materials have attracted much attention as a means to achieve light confinement in regions with cross sectional dimensions smaller than $\lambda/2n$; however, this increased confinement comes at the cost of increased fundamental optical loss due to absorption by the metal [7, 8, 9, 10, 11]. The fundamental trade-off between confinement and loss in SPP waveguides limits their application particularly for long-range propagation and high quality factor resonant cavities. In this Chapter we show how utilizing nanoscale dielectric discontinuities allows one to decrease the effective mode volume several orders of magnitude below a cubic half-wavelength in dielectric materials [1].

[1] Portions of this chapter are reproduced with permission from [12]

2.2 Light-Matter Interaction in Dielectric Nanostructures

To understand how the mode volume can be reduced it is first necessary to formulate a meaningful definition. Since the purpose of nanoscale light confinement is to increase the interaction between light and matter we must chose a specific light-matter interaction and from there derive the appropriate effective mode volume (V_{eff}). In general, the definition of V_{eff} should vary depending on the light-matter interaction of interest. The most commonly used definition of V_{eff} (and the one we shall use here) relates to the change in the spontaneous emission rate for an atom placed in an optical resonant cavity. This is known as the Purcell effect [13]. We will follow a derivation of V_{eff} similar to [3] with a few corrections.

The Purcell factor (a measure of the spontaneous emission rate enhancement) for an emitter in a resonant cavity can be derived directly from Fermi's golden rule [3, 14]:

$$\Gamma = \frac{2\pi}{\hbar^2} \int_{\infty}^{\infty} \langle |\vec{p_a} \cdot \alpha \vec{E}(\vec{r_e})|^2 \rangle \rho_c(\omega) \rho_e(\omega) d\omega \tag{2.1}$$

Where $\rho_c(\omega)$ is the density of photon modes in the cavity, $\rho_c(\omega)$ is the mode density for the dipole transition (material emission spectrum), $\vec{p_a}$ is the atomic dipole moment, $\vec{E}(\vec{r_e})$ is the electric field at the location of the emitter normalized by a factor $\alpha^2 \equiv \frac{\hbar\omega}{2} \frac{4\pi}{\int_{\infty} \varepsilon(\vec{r}) \vec{E}^2(\vec{r}) d^3r}$ to the zero point energy. From Eq. (2.1) we see that for a given emitter with ($\rho_e(\omega)$), there are two ways to increase the spontaneous emission rate. First one can increase the cavity mode density ($\rho_c(\omega)$). This is commonly measured as an increase in the cavity quality factor ($Q = \omega_0/\Delta\omega$) where ω_0 is the resonant frequency and $\Delta\omega$ is resonant linewidth. Secondly one can increase the value of the normalized electric field at the emitter

($\alpha\vec{E}(\vec{r_e})$). As we will show below, this amounts to decreasing the effective volume of the electromagnetic energy in the resonant mode (V_{eff}). Thus the common figure of merit for resonant cavities is the ratio Q/V_{eff} [4, 3, 15]. This can be seen from the Purcell factor (F_p) in Eq. (2.2). From Eq. (2.1) when the emitter is paced at the peak of the electric field and the cavity resonant frequency equals the peak emission frequency (ω_e), the ratio of spontaneous emission rate in the cavity compared to bulk can be written as [13, 16, 3]

$$F_p = \frac{\Gamma}{\Gamma_0} = \frac{6Q(\lambda/2n)^3}{\pi^2}\frac{\epsilon(\vec{r}_{max})\max[|\vec{E}(\vec{r})|^2]}{\int \epsilon(\vec{r})|\vec{E}(\vec{r})|^2 d^3r} = \frac{6Q(\lambda/2n)^3}{\pi^2 V_{eff}} = \frac{6Q}{\pi^2 \tilde{V}_{eff}} \tag{2.2}$$

where n is the index of refraction at the peak field ($\vec{r}_{max}$). We define the normalized unitless effective mode volume as:

$$\tilde{V}_{eff} = V_{eff}\left(\frac{2n(\vec{r}_{max})}{\lambda}\right)^3 = \frac{\int \epsilon(\vec{r})|\vec{E}(\vec{r})|^2 d^3r}{\epsilon(\vec{r}_{max})\max[|\vec{E}(\vec{r})|^2]}\left(\frac{2n(\vec{r}_{max})}{\lambda}\right)^3 \tag{2.3}$$

where $\vec{r}_{max}$ is the location of the maximum squared field. It is important to note that this definition of V_{eff} differs from most previously published definitions in that $\epsilon(\vec{r}_{max})$ sits outside of the $\max[]$ operator. Because most previous derivations consider light to be confined within a homogeneous material (ϵ is independent of $\vec{r}$) this term is usually found within the $\max[]$ operator. When dealing with nanostructured material as we are here, one must remove this term from the $\max[]$ operator. It is also important to note that Eq. (2.2) is valid under the condition that the cavity's resonance linewidth is greater than the emission linewidth of the active element [3, 16]. When the resonance linewidth of the cavity is much smaller than that of the emitter (as is the case at room temperature for high-Q cavities in rare-earth-doped materials), $\rho_c(\omega)$ in Eq. (2.1) is replaced by $\delta(\omega_e)$. In this regime the "material Q" ($Q_m = \omega_e/\Delta\omega_e$ where $\Delta\omega_e$ is the linewidth of the emitter) replaces the cavity Q in Eq. (2.2) [16]. Thus increasing the cavity Q has no effect on the spontaneous emission rate. The only means of increasing the spontaneous emission rate in this regime is to decrease $\tilde{V}_{eff}$.

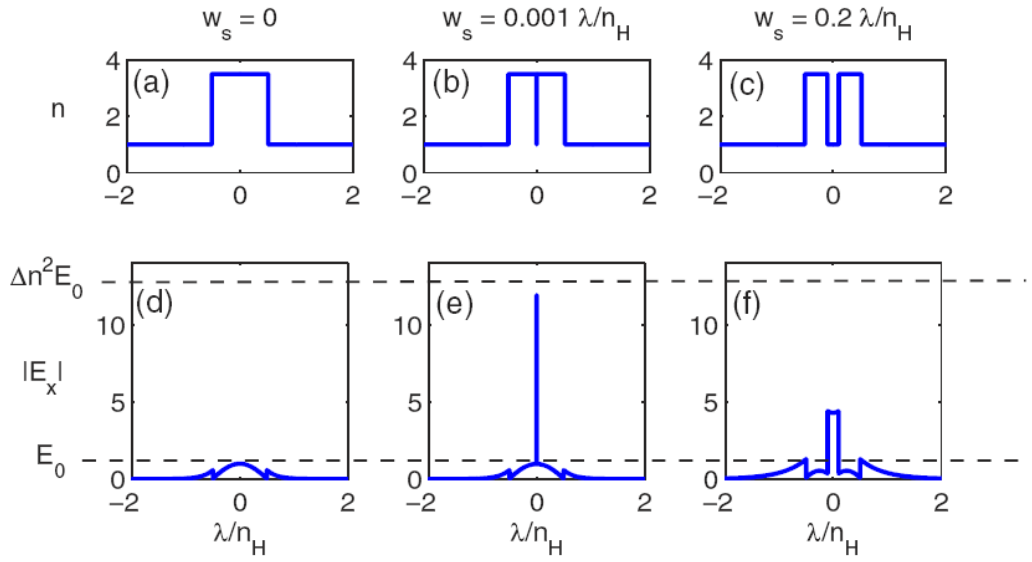

Figure 2.1: a-c: The index profile for the slab waveguide with embedded low index slot regions of various slot widths (w_s) d-f: The field distribution of the fundamental mode in the slab waveguide for various values of w_s. The electric field is polarized normal to the interface. E_0 is the maximum value of the electric field for the slab with no slot and Δn is the ratio n_H/n_L.

2.3 Mode Volumes Below the "Diffraction Limit" in Dielectric Optical Resonators

As shown in the previous section a reduction $\tilde{V}_{eff}$ can be achieved by simply increasing the maximum value of the normalized squared field $\left(\frac{max[|E(\vec{r})|^2]}{\int_\infty \epsilon(\vec{r})|E(\vec{r})|^2 d^3r}\right)$ in Eq. (2.3).

We can achieve this increase in the normalized maximum field by using sub-wavelength-sized dielectric material discontinuities [17]. For example, consider a one dimensional high index contrast slab (Fig. 2.1(a)). Fig. 2.1(d) shows the field distribution of the fundamental mode in this structure, for an electric field polarized normal to the interface. One can introduce an infinitesimal low in-

dex slot at the location of peak intensity oriented perpendicular to the electric field polarization. Fig. 2.1(b) shows an example of this slot introduced in a one dimensional slab. We recall from Maxwell's equations that the normal component of the electric displacement (D) is continuous across the boundary of two dielectrics thus $\epsilon_L E_L = \epsilon_H E_H$ where L and H denote the low and high refractive index regions respectively. Fig. 2.1(e) shows the new eigenmode of the slab waveguide after the introduction of a narrow slot. The unitless effective mode volume in a waveguide with an infinitesimal slot is given by:

$$\tilde{V}^*_{eff} = \frac{\int \epsilon(\vec{r})|E(\vec{r})|^2 d^3\vec{r}}{\epsilon_L |\epsilon_H/\epsilon_L E_0|^2} \left(\frac{2n_L}{\lambda}\right)^3 \tag{2.4}$$

where E_0 is the maximum value of the field in the high index before introducing the slot. The infinitesimal slot has a negligible effect on the integral in the numerator; therefore the ratio of unitless mode volumes, or the Purcell factors (see Eq. (2.2)), before and after the introduction of a slot is approximately given by

$$\frac{F_p}{F^*_p} = \frac{\tilde{V}^*_{eff}}{\tilde{V}_{eff}} \approx \left(\frac{\epsilon_L}{\epsilon_H}\right)^{5/2} \tag{2.5}$$

The above decrease in effective mode volume is wavelength independent and can represent more than an order of magnitude reduction. For example using dielectric materials such as air ($\epsilon = 1$) and amorphous Silicon in the infrared ($\epsilon = 13.9$) results in a reduction in $\tilde{V}_{eff}$ by a factor of over 700. Due to the normalization to the bulk spontaneous emission rate in the Purcell factor, the radiative decay rate in the cavity is proportional to the Purcell factor times the bulk index. This bulk index is different for the cavity with and without the slot since the emitter is embedded in different bulk materials (n_H for the cavity without the slot and with n_L for the cavity with the slot). Thus the increase in the spontaneous emission rate at the peak field resulting from the introduction

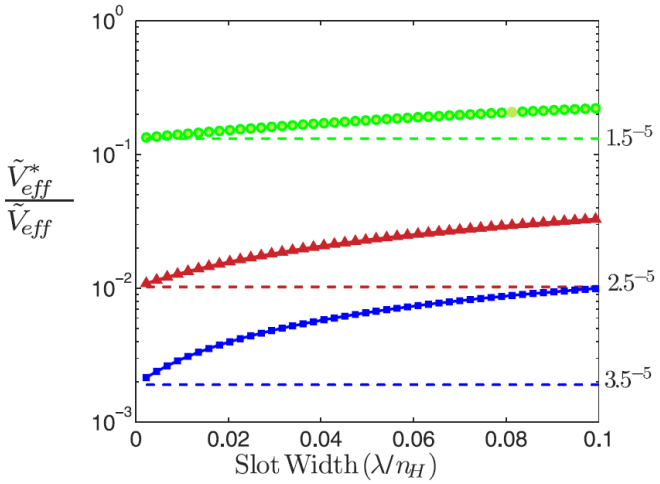

Figure 2.2: The ratio of the effective mode volume of a slot waveguide compared to a slab waveguide for $\Delta n = 1.5$ (circles),$\Delta n = 2.5$ (triangles), and $\Delta n = 3.5$ (squares), where Δn is the ratio of high to low refractive indices. The slab thickness is λ/n_H.

of the slot is given as:

$$\frac{\Gamma^*}{\Gamma} = \frac{\tilde{V}_{eff}}{\tilde{V}^*_{eff}} \left(\frac{n_L}{n_H}\right) \approx \left(\frac{\epsilon_H}{\epsilon_L}\right)^2 \tag{2.6}$$

Field enhancement in the low index region of slot waveguides has recently been demonstrated experimentally in [18]. In Figs. 2.1(e) and 2.1(f) we show the field distributions in a slab waveguide with two different slot widths shown in Figs. 2.1(c) and 2.1(d). As the slot width increases the mode no longer resembles the original mode with a discontinuity, but becomes more confined to either side of the high index material. We plot in Fig. 2.2 $\frac{\tilde{V}^*_{eff}}{\tilde{V}_{eff}}$ as a function of slot width for a cavity in which the field is confined in a slab waveguide of width λ/n_H for various index contrasts ($\Delta n = \sqrt{\epsilon_H/\epsilon_L}$). From Eq. (2.5) we see this ratio is equivalent the ratio of Purcell factors in the non-slot and slot cavities. As the width of the slot narrows the relative decrease in V_{eff} approaches the dashed lines which represent the theoretical limit of Δn^{-5} given in Eq. (2.5).

In order to analyze the effect of the reduced mode volume on the Purcell

effect, we embed the waveguide with a slot in a quasi-one-dimensional microcavity with $Q \sim 10^2$. The microcavity shown in Fig. 2.3(b) is a 460 nm x 260 nm buried waveguide with refractive index of 3.48 and a cladding index of 1.46 [19]. The 1D photonic crystal on either side of the cavity consists of five 200 nm diameter holes spaced 360 nm center-to-center with a refractive index of 1.46. The cavity length at the center of the structure is 880 nm between the hole centers. The slot at the center of the cavity in Fig. 3(a) has a refractive index of 1.0 which is similar to recently reported fabrication [18]. Fig. 2.3(b) shows the squared magnitude of the electric field at the resonant wavelength of 1556 nm in the cross-sectional plane at the waveguide center (z = 130 nm). Fig. 2.3(a) shows the same cavity after the introduction of a 20 nm wide slot with a refractive index of 1.0 in the cavity region. The magnitude of the electric field is determined using 3D finite difference time domain (FDTD) technique to calculate the resonant mode in each of the cavities (note that a shift of the resonance occurs, from 1556 nm to 1431 nm, when the slot is introduced due to the resulting decrease in the effective index of the cavity). Using Eq. (2.3) and the results of the 3D FDTD we calculate a decrease in V_{eff} from approximately $3.34(\lambda/2n)^3$ in Fig. 2.3(b) to $0.042(\lambda/2n)^3$ in Fig. 2.3(a). From Eq. (2.5) this corresponds to nearly an 80-fold increase in the Purcell factor and an increase in spontaneous emission rate for atoms in the cavity center by more than a factor of 20. Note from Eqs. (2.5) and (2.6) that the increase in the Purcell factor is larger than the increase in the spontaneous emission rate by a factor of n_H/n_L. The increase is smaller than the one predicted from Eqs. (2.5) and (2.6) due to the finite width of the slot. A smaller slot in the same materials could yield over 500-fold increase in the Purcell factor. The Q factor (determined by measuring the intensity decay rate of the cavity mode ($1/\tau_p$) where $Q = \omega\tau_p$ [20]) is slightly lowered by the

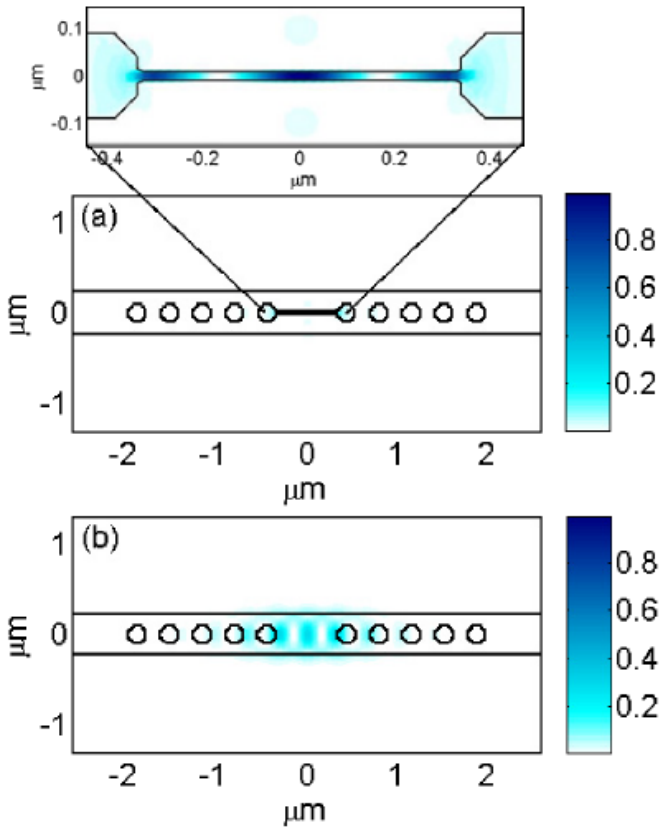

Figure 2.3: (a) $|E|^2$ field spatial distribution from 3D FDTD in the a cavity based a on buried waveguide with an embedded low index slot at its resonant wavelength of 1431.3 nm. (b) $|E|^2$ field spatial distribution from 3D FDTD in a quasi-1D microcavity based on a buried waveguide without a slot for the resonant wavelength of 1556.4 nm.

introduction of the slot, decreasing from 305 to 175. Optimization of the cavity to better confine the new mode could be used to raise the new Q factor [21].

Note that the Purcell formalism described above in Eqs. (2.1) and (2.2) is valid in the regime in which the field does not vary significantly over the size of the emitter. To verify the proposed structure is indeed in this regime we compare the field decay length in the slot ($1/\gamma_s$) to the size of the emitter. Taking λ to be 1.55 μm, for slots ranging from 0.001 to 0.2 $\lambda/2n_H$, $1/\gamma_s$ is about three

order of magnitude larger than the size of an atom or ion-based emitters. Thus these structures are well within the regime described by Eq. (2.1) [17]. Also note that throughout the paper we assume that the coupling of the cavity to the emitters is in the weak coupling regime, i.e., the photon lifetime (τ_p) is much smaller than the inverse of the emitter-cavity coupling frequency. In the present work, for realistic sub-micron cavities with $Q \sim 10^3$ ($\tau_p \sim 0.8$ps) we are well within this regime.

2.4 Summary

In this chapter we have shown that because the local value of the electric field is responsible for light-matter interaction, V_{eff} can be decreased by simply enhancing the local electric field value. This can be achieved by utilizing the electric field discontinuity at dielectric interfaces. This allows one to create confined optical modes with a V_{eff} several orders of magnitude below what was believed to be the $(\lambda/2n)^3$ "diffraction limit."

This principle of reduction of V_{eff}, well below the dimensions of the wavelength of light can be applied to nearly every existing microcavity resonator to enhance not only light emission but also non-linear effects. Examples of emitters embedded in low index media that could be used are gas-phase atoms and rare-earth doped oxides. Such a reduction can enable the demonstration of effective mode volumes on the order of $10^{-2}(\lambda/2n)^3$ or smaller and increase the Purcell factor by orders of magnitude. This technique may enable new experiments in cavity Quantum Electrodynamics, ultra-sensitive single atom detection, and low threshold lasers.

BIBLIOGRAPHY

[1] E. Ozbay, "Plasmonics: Merging Photonics and Electronics at Nanoscale Dimensions," Science **311,** 189–193 (2006).

[2] M. Born and E. Wolf, *Principles of Optics: Electromagnetic Theory of Propagation, Interference and Diffraction of Light*, 7th ed. (Cambridge University Press, 1999), p. 986.

[3] *Confined Electrons and Photons: New Physics and Applications*, E. Burstein and C. Weisbuch, eds., (Plenum Press, 1994).

[4] K. J. Vahala, "Optical microcavities," Nature **424,** 839–846 (2003).

[5] S. A. Maier, P. G. Kik, H. A. Atwater, S. Meltzer, E. Harel, B. E. Koel, and A. A. Requicha, "Local detection of electromagnetic energy transport below the diffraction limit in metal nanoparticle plasmon waveguides," Nat Mater **2,** 229–232 (2003).

[6] E. Feigenbaum and M. Orenstein, "Optical 3D cavity modes below the diffraction-limit using slow-wave surface-plasmon-polaritons," Opt. Express **15,** 2607–2612 (2007).

[7] V. M. Shalaev and S. Kawata, *Nanophotonics with Surface Plasmons* (Elsevier Science, 2007).

[8] W. L. Barnes, A. Dereux, and T. W. Ebbesen, "Surface plasmon subwavelength optics," Nature **424,** 824–830 (2003).

[9] S. I. Bozhevolnyi, V. S. Volkov, E. Devaux, J.-Y. Laluet, and T. W. Ebbesen, "Channel plasmon subwavelength waveguide components including interferometers and ring resonators," Nature **440,** 508–511 (2006).

[10] L. Chen, J. Shakya, and M. Lipson, "Subwavelength confinement in an integrated metal slot waveguide on silicon," Optics Letters **31,** 2133–2135 (2006).

[11] J. A. Dionne, H. J. Lezec, and H. A. Atwater, "Highly confined photon transport in subwavelength metallic slot waveguides," Nano Letters **6,** 1928–32 (2006).

[12] J. T. Robinson, C. Manolatou, C. Long, and M. Lipson, "Ultrasmall mode volumes in dielectric optical microcavities," Physical Review Letters **95,** 143901–1 (2005).

[13] E. M. Purcell, "Spontaneous emission probabilites at radio freqencies," Phys. Lett. **69,** 681 (1946).

[14] B. Gayral, J. M. Gérald, A. Lemaître, C. Dupuis, L. Manin, and J. L. Pelouard, "High-Q wet-etched GaAs microdisks containing InAs quantum boxes," App. Phys. Lett. **75,** 1908–1910 (1999).

[15] Y. Akahane, T. Asano, B.-S. Song, and S. Noda, "High-Q photonic nanocavity in a two-dimensional photonic crystal," Nature **425,** 944 (2003).

[16] R. Coccioli, M. Boroditsky, K. W. Kim, Y. Rahmat-Samii, and E. Yoblonovitch, "Smallest possible electromagnetic mode volume in a dielectric cavity," IEE Proceedings Optoelectronics **145,** 391 (1998).

[17] V. R. Almeida, Q. Xu, C. A. Barrios, and M. Lipson, "Guiding and confining light in void nanostructure," Optics Letters **29,** 1209–1211 (2004).

[18] Q. Xu, V. R. Almeida, R. Panepucci, and M. Lipson, "Experimental demonstration of guiding and confining light in nanometer-size low-refractive-index material," Optics Letters **29,** 1626–1628 (2004).

[19] J. S. Foresi, P. R. Villeneuve, J. Ferrera, E. R. Thoen, G. Steinmeyer, S. Fan, J. D. Jannopoulos, L. C. Kimerling, H. I. Smith, and E. P. Ippen, "Photonic-bandgap microcavities in optical waveguides," Nature **390,** 143 (1997).

[20] C. Pollock and M. Lipson, *Integrated Photonics* (Kluwer Academic, 2003).

[21] P. Lalanne, S. Mias, and J. Hugonin, "Two physical mechanisms for boosting the quality factor to cavity volume ratio of photonic crystal microcavities," Optics Express **12,** 458–467 (2004).

CHAPTER 3

MEASUREMENT OF NANOSCALE LIGHT CONFINEMENT

3.1 Introduction

While evidence of the type of nanoscale light confinement described in Chapter 1 can be inferred from several experiments [1, 2, 3, 4], direct observation of light confinement below $\lambda/2n$ in dielectric materials requires the development of novel Near field Scanning Optical Microscopy (NSOM) techniques.

Traditional near field measurement techniques are incapable of this measurement since they suffer from either poor aperture-limited resolution or poor collection efficiency. Aperture NSOM techniques typically use tapered optical fibers (often metal coated) to collect light from the evanescent field through a sub-wavelength sized aperture [5, 6, 7, 8]. Measuring the power collected as a function of probe position creates an image of the local evanescent field. This technique has been used to observe confinement and guiding in micron-sized semiconductor waveguides and transverse optical decay lengths as small as $\lambda/7$ in the near infrared have been reported [8]. Performing these measurements is challenging since NSOM probes are typically metal coated and thus the probe size is about twice that of the physical aperture. This prevents the aperture from moving close to the sides of the waveguide to measure short transverse optical decay lengths. Additionally, the resolution of these NSOM measurements is limited by the aperture size which is typically no smaller than $\lambda/10$. This lower bound on the aperture size relates to the transmission through sub-wavelength-sized holes which falls as $(r/\lambda)^4$ where r is the aperture radius [9]. Apertureless NSOM (a-NSOM), also known as scattering NSOM (s-NSOM), of-

fers several advantages over traditional aperture NSOM. In s-NSOM a sharp metal or dielectric probe scatters some of the local evanescent field into the far field where it can be detected [10, 11, 12]. Compared to aperture NSOM probes, s-NSOM probes are generally more robust, inexpensive and easy to fabricate. The main advantage of such systems, relative to NSOM, is that since light is not collected through the probe, probe diameters can be orders of magnitude smaller than aperture NSOM probes and still generate measurable signals. This greatly increases the spatial resolution of the optical measurements. Since the entirety of the s-NSOM probe is sensitive to the local field (unlike metal coated NSOM probes which only collect light through the aperture at the probe center), it can be used to measure the field very close to the sides of the waveguide. Applying the s-NSOM technique to photonic devices, however, is challenging. Scattered light is often collected in the far field from multiple sources including defects along the waveguide. Separating light scattered from the probe and that scattered from these defects requires complex heterodyne interferometric measurement techniques [13, 2] similar to those used in time-resolved NSOM measurements [3]. Additionally, scattering from sharp probes is inherently a highly polarization-sensitive process [14, 15, 16, 17] and cannot measure the field confined in nanoscale slot geometries.

In this chapter we present two new types of apertureless NSOM: Transmission-based Near field Scanning Optical Microscopy (TraNSOM), and interferometric Transmission-based Near field Scanning Optical Microscopy (i-TraNSOM) which offer both the high resolution and high collection efficiency necessary to characterize nanoscale light confinement in photonic structures. We show that the TraNSOM technique like the s-NSOM technique is highly polarization sensitive while the i-TraNSOM technique, unlike previously demon-

strated NSOM techniques measures, measures all polarizations equally.

Using the TraNSOM technique we measure sub-100 nm the transverse optical decay lengths for near-infrared (IR) light. At the time of this publication these transverse decay lengths, shorter than $\lambda/15$, are the shortest values to be measured[14].

Using the i-TraNSOM technique we directly measure the spatial distribution of light with a wavelength of 1525 nm confined to an 85 nm ($\lambda/15$) air gap in a silicon waveguide as described in Chapter 1. This represents the first direct measurement of light confinement below $\lambda/2n$ in dielectric structures[1].

3.2 Transmission-based Near-field Scanning Optical Microscopy: TraNSOM

3.2.1 Introduction

Unlike previously demonstrated NSOM techniques, Transmission-based Near field Scanning Optical Microscopy (TraNSOM) offers both high resolution measurement and high collection efficiency, eliminating the need for interferometric heterodyne measurements or far-field collection optics. We achieve this high resolution and improved collection efficiency by measuring the transmission of light through a device where the mode is disturbed by a metallic Atomic Force Microscope (AFM) probe. By disturbing the mode, some of the light confined in the guided mode is coupled to radiation modes (scattering) or absorbed by

[1]Portions of this chapter are reproduced with permission from [12]

the probe. The amount of scattering and absorption is related to the local magnitude of the optical near field. Thus, by measuring the transmission as we scan the AFM probe, we construct an image of the optical near field. In contrast to previous s-NSOM techniques we achieve much larger collection efficiency since almost all the light scattered and absorbed contributes to the measured drop in transmission.

Historically, the TraNSOM technique was first reported in [14] and independently in [4], although subsequent implementations have sometimes been referred to as T-SNOM [18] and SNOM *interaction-scanning mode*[19].

3.2.2 Experimental Setup

The experimental TraNSOM setup consists simply of a photonic chip bonded to input and output optical fibers and placed under a AFM. In our setup we use a commercial Dimension 3100 AFM in an acoustic enclosure to reduce optical noise associated with vibration of the input and output fibers. A schematic of this setup is shown in Fig. 3.1. As a light source we use about 80 mW of unpolarized amplified spontaneous emission (ASE) output from an Erbium Doped Fiber Amplifier (EDFA) sent through a tunable grating filter set to 1532 nm to match the peak of the ASE. The output of the filter is sent through an in-line polarization controller to a cleaved optical fiber which is coupled to the waveguide input and bonded to the microscope slide using a low-shrink UV curable epoxy (Dymax OP-4-20641). A cleaved optical fiber is also coupled to the waveguide output and bonded to the microscope slide. The output fiber is sent to a photodetector and power meter. We then place the packaged photonic in the AFM to

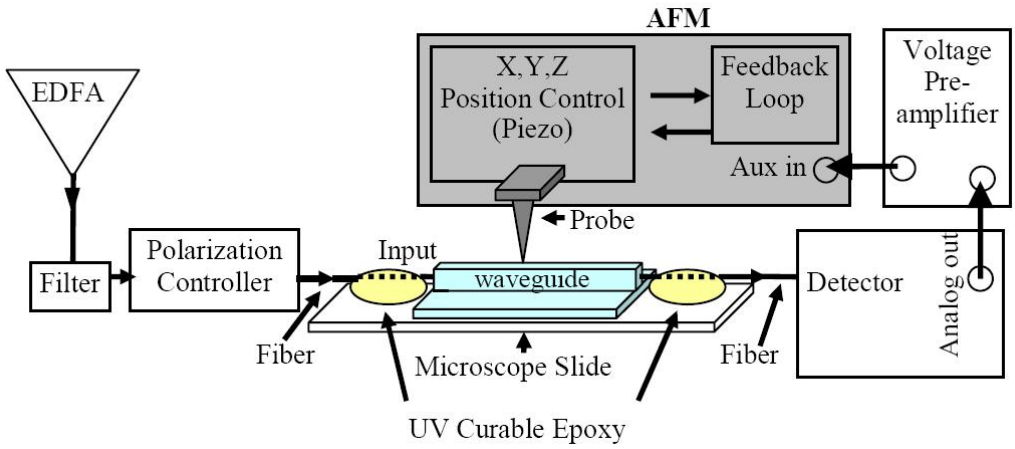

Figure 3.1: Experimental setup for TraNSOM measurements

be imaged. Using a PtIr coated probe from Nanosensors we image the device in intermittent contact or "tapping" mode. The analog output of the power meter is sent to voltage pre-amplifier with a 30 Hz low pass filter to reduce high frequency noise. The output of the voltage pre-amplifier is sent to the auxiliary input of the AFM which simultaneously records the topography and transmission through the device as the probe is scanned over the sample.

3.2.3 Interpreting the TraNSOM Signal

To quantitatively understand what is measured by the change in transmission, we analyze the scattering and absorption induced by the near-field probe. According to scattering theory [7, 3], to first order the power scattered and absorbed is the result of damped dipole radiation induced by the incident electric field. The magnitude of the induced dipole depends on the probe material, geometry, and the relative polarization and magnitude of the incident electric field. By modeling the probe as a cone, one can choose the principal axes of the

cone as a Cartesian basis such that $\hat{y}$ is along the cone axis and $\hat{x}$ and $\hat{z}$ are in the plane perpendicular to the cone axis (see Fig. 3.1). Since the polarizability is diagonal in this basis we can write the total power lost P_{ext} as the sum of the power lost to absorption P_{abs} and scattering P_{sca}:

$$\begin{aligned} P_{ext} &= P_{abs} + P_{sca} && (3.1) \\ &= \frac{1}{2}\sqrt{\frac{\mu_0}{\epsilon_0}} \int_A \left(Q_{ext\perp} \left|E_x\right|^2 + Q_{ext\parallel} \left|E_y\right|^2 + Q_{ext\perp} \left|E_z\right|^2 \right) da, && (3.2) \end{aligned}$$

where A is the cross sectional area of the scattering probe, $Q_{ext\perp}$ is the extinction efficiency for the field perpendicular to the probe axis, and $Q_{ext\parallel}$ is the extinction efficiency for the field parallel to the probe axis. The extinction efficiency is defined as the scattering cross section plus the absorption cross section divided by the geometric cross section [3]. This is equivalent to the total power scattered and absorbed normalized to the power incident on the probe. Scattering efficiencies much less than one indicate that light passes relatively unimpeded through the object. It has been shown by several sources [20, 21, 22] that the probe-field interaction is dominated by the polarization component along the tip axis. Appling this condition ($Q_{ext\parallel} >> Q_{ext\perp}$) we can approximate the total power loss as:

$$P_{ext} \approx Q_{ext\parallel} \frac{1}{2}\sqrt{\frac{\mu_0}{\epsilon_0}} \int\limits_A \left|E_y\right|^2 da, \tag{3.3}$$

We now relate the measured transmission signal to the local electric field. We can write the transmitted power measured at the detector (P_{out}) in terms of the power input from the source (P_{in}), the total transmittance between the source

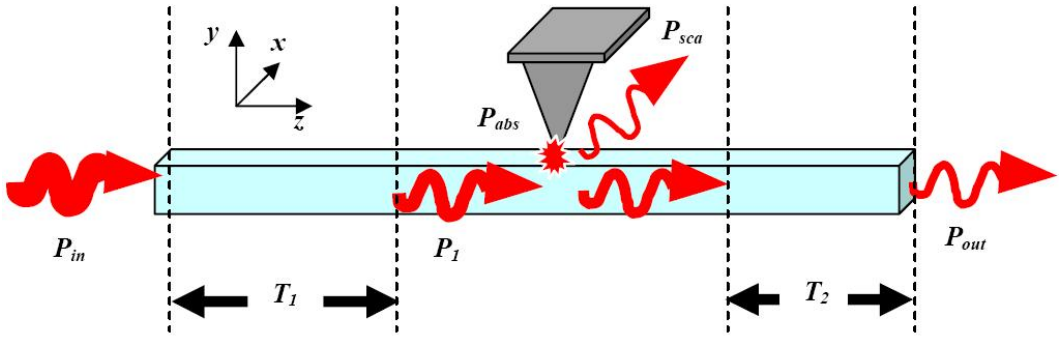

Figure 3.2: Model of the TraNSOM measurement where P_{in} is the power input from the source, T_1 is the transmittivity between the source and the probe, P_{abs} is the power absorbed from by the probe, P_{sca} is the power scattered by the probe, T_2 is the transmittivity between the probe and the detector, and P_{out} is the power detected at the output

and the probe position (T_1) and the probe position and detector (T_2), and the power lost to absorption and scattering by the probe (P_{ext}) (see Fig. 3.2) as

$$P_{out} = T_1 T_2 P_{in} \left(1 - \frac{P_{ext}}{P_1}\right), \tag{3.4}$$

where we have defined the power in the waveguide immediately before the probe as $P_1 \equiv T_1 P_i n$ which is equivalent to an integral of the pointing flux through an infinite plane just before the probe . In the absence of the probe the measured power follows from $\left(P_1 = \frac{1}{2}\int_\infty Re[\overrightarrow{E} \times \overrightarrow{H}^*] \cdot \hat{z} da\right)$ Eq. 3.4:

$$P_{out0} = T_1 T_2 P_{in}. \tag{3.5}$$

We define the measured signal (ΔT) in terms of the measured transmission with and without the probe:

$$\Delta T \equiv 1 - \frac{P_{out}}{P_{out0}} = \frac{P_{ext}}{P_1} \approx \frac{Q_{ext\|}\sqrt{\frac{\mu_0}{\epsilon_0}}\int_A |E_y|^2\, da}{\int_\infty \mathrm{Re}[\overrightarrow{E} \times \overrightarrow{H}^*] \cdot \hat{z} da}. \tag{3.6}$$

Therefore the measured quantity is related to the square of the local electric field normalized to the local power in the mode.

3.2.4 Measurement of Nanoscale Optical Decay Lengths

To test the TraNSOM technique we fabricate sub-micron scale silicon waveguides on an SOI wafer with a 3 micron buried oxide layer. Using a series of thermal oxidation steps the silicon is thinned to a thickness of about 250 nm covered with about 150 nm of thermal oxide. The waveguides are then patterned using electron beam lithography and etched using inductively coupled plasma etching leaving a silicon core approximately 520 nm wide at its base and 250 nm tall covered on top with about 150 nm of thermal oxide. A side wall angle of 79^o is estimated from the waveguide width at the top and bottom measured using a scanning electron microscope. The waveguides are air clad with the exception of the input and output where we adiabatically narrow the width of the waveguides to about 120 nm and cover them with 2 micron tall by 8 micron wide waveguides made of photoresist which we fabricate using contact lithography. This increases the coupling efficiency and selectivity for the quasi-TE mode [4, 23]. Using an in-line polarization controller to minimize or maximize the output we can selectively excite either the quasi-TM or quasi-TE mode respectively. We measure a total transmittance for quasi-TE to be about 20 times larger than for quasi-TM.

Using the experimental setup described in Section 3.2.2 we measure the to-

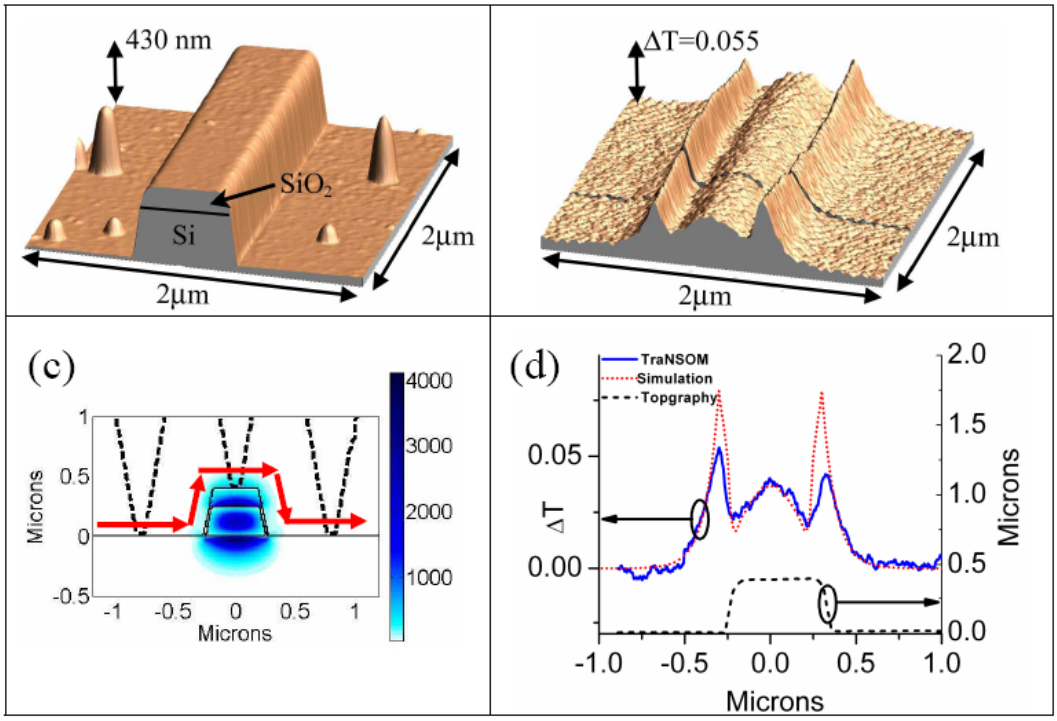

Figure 3.3: (a) AFM image of the SOI waveguide (b) simultaneously recorded TraNSOM image of the fundamental quasi-TM mode (c) simulated major component ($|E_y|^2$) of the fundamental quasi-TM mode. Dashed lines show the outline of the probe at three positions. Bold arrows show the path of the probe convolution. (d) Solid line shows the measured TraNSOM signal taken along the solid line in (b). Dashed line shows the simultaneously measured topography. Dotted line shows the probe-field convolution for all three polarization components according to Eq. 3.1 with $Q_{ext\parallel} = 6.4$ and $Q_{ext\perp} = 0.08$.

pography and optical mode of a sub-micron-sized SOI waveguide. Fig. 3.3(a) and (b) show the simultaneously recorded topographic and TraNSOM image of the quasi-TM mode scanned over a 2x2 micron region. We use a 2-line interpolation in WSxM to help remove high frequency noise in the images. Notice that the small pillars to the left and right of the waveguide resulting from micro-masking in the fabrication process do not appear in the optical image since the optical field is confined only to the waveguide.

We verify the measurement technique by comparing the measured mode profile to calculated results and determine the transverse optical decay length for the quasi-TM mode. Since the probe is most sensitive to the field polarized along the cone axis, we plot the major component of the quasi-TM mode ($|E_y|^2$) in Fig. 3.3(c) calculated using a finite element mode solver and normalized to unit power. The dashed lines outline the probe cross section at three different positions as it is scanned over the waveguide. The probe dimensions are taken from the manufacturer specifications of a 10^o half angle and 25 nm radius of curvature. Fig. 3.3(d) shows a cross section of the measured ΔT (solid blue) taken along the line shown in Fig. 3.3(b). The simultaneously measured topography is shown as the dashed black line. The dotted red line in Fig. 3.3(d) shows the convolution of the probe cross section (A) with the simulated mode profile shown in Fig. 3.3(c). This convolution was performed for all three field components and weighted by and (given below) according to Eq. 3.1. We measure the transverse optical decay length by analyzing the evanescent field measured to the left and right of the waveguide. We fit the evanescent field in Fig. 3.3(d) to an exponential which decays as $\exp(-|x|/\xi)$ where x is the distance from the waveguide core and ξ is the transverse optical decay length. From the fit we measure this quantity to be 100 ± 12 nm ($\sim \lambda/15$), where the error represents the 95% confidence interval. This result compares well with the convolution of the probe with the calculated mode profile which predicts a transverse optical decay length of 70 nm.

To confirm we are indeed predominantly measuring the field polarized along the probe axis, we compare a measurement of the quasi-TE mode with its calculated minor field component ($|E_y|^2$). Fig. 3.4(a) and (b) show the simultaneously recorded topographic and TraNSOM image of the quasi-TE mode

scanned over the same 2x2 micron region as Fig. 3.3(a) and (b). Fig. 3.4(c) shows the minor component for the quasi-TE mode normalized to unit power and the path of the probe convolution. Note that since this is the minor field component, the magnitude of the field is ten times smaller than the major component of the quasi-TM mode (Fig. 3.3(c)) and concentrated near the waveguide corners which is typical in high-index-contrast waveguides. This is in agreement with the measured mode profile in Fig. 3.4(b) which shows the field is concentrated near the edges of the waveguide and shows a ten fold decrease in the magnitude of the measured signal compared to the quasi-TM mode (note the scale difference of ΔT in Figs. 3.3(b) and 3.4(b)). Fig. 3.4(d) shows a cross section of the measured ΔT (solid blue) taken along the line shown in Fig. 3.4(b). The simultaneously measured topography is shown as the dashed black line. The dotted red line in Fig. 3.4(d) shows the convolution of the probe cross section (A) with the simulated mode profiles shown in Fig. 3.4(c) weighted by $Q_{ext\|}$ and $Q_{ext\perp}$. Similarly to the analysis of the major field component of the quasi-TM mode, we analyze the transverse optical decay length of the *minor* field component ($|E_y|^2$) of the quasi-TE mode. Fitting the exponential decay to the left and right of the waveguide we measure the minor field transverse optical decay length to be 49 ± 9 nm ($\sim \lambda/30$), which compares very well with the 46 nm decay length predicted by our simulations. To our knowledge, these transverse optical decay lengths for the quasi-TM and quasi-TE modes are the shortest measured for waveguides in the near infrared and are a result of the high index contrast between Si and air.

We determine the quantitative extinction efficiency of the probe for two orthogonal polarizations by fitting the measured data to the calculated probe-field convolution. The values of $Q_{ext\|} = 6.4 \pm 0.5$ and $Q_{ext\perp} 0.08 \pm 0.05$ are calculated

by performing a least squares fit of the simulated probe-field convolution to the measured data simultaneously for the quasi-TE and quasi-TM data over the regions that are topographically flat. The results of this fit are plotted as the dotted lines in Figs. 3.3(d) and 3.4(d). The fact that $Q_{ext\|}$ is two orders of magnitude larger than $Q_{ext\perp}$ confirms the assumption in Section 3.2.3 that for this probe geometry, the field along the probe axis (E_y) dominates the measured signal (i.e.: $Q_{ext\|} >> Q_{ext\perp}$). Note that the simulated data over-estimates the probe-field interaction near the upper corners of the waveguide since the fabricated waveguide has rounded corners with about a 60 nm radius of curvature, as seen in the AFM images (Figs. 3.3(a) and 3.4(a)), which keep the probe farther from the waveguide core than is predicted from the sharp cornered simulations shown in Figs. 3.3(c) and 3.4(c).

3.2.5 Summary

In this section we have described a novel technique for measuring sub-micron optical features of highly confined photonic structures. Using this new high resolution apertureless technique we measure a transverse optical decay length for the quasi-TM mode of $\lambda/15$ which, to our knowledge, is the shortest decay length measured in near infrared waveguides. As opposed to previous near field measurement techniques, this technique enables both high collection efficiency and high resolution and therefore does not require any far field collection optics, interferometric measurements, or expensive aperture probes.

Because this technique, as we have shown, is highly polarization sensitive, to locally measure both polarizations of the optical mode we must turn to a new

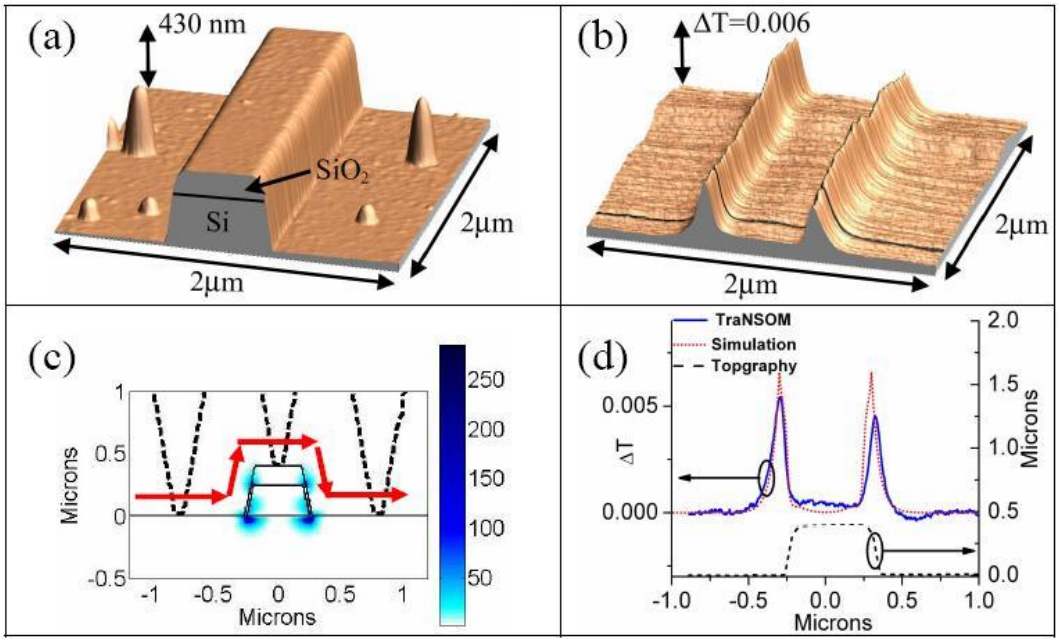

Figure 3.4: (a) AFM image of the SOI waveguide (b) simultaneously recorded TraNSOM image of the fundamental quasi-TM mode (c) simulated minor component ($|E_y|^2$) of the fundamental quasi-TE mode. Dashed lines show the outline of the probe at three positions. Bold arrows show the path of the probe convolution. (d) Solid line shows the measured TraNSOM signal taken along the solid line in (b). Dashed line shows the simultaneously measured topography. Dotted line shows the probe-field convolution for all three polarization components according to Eq. 3.1 with $Q_{ext\parallel} = 6.4$ and $Q_{ext\perp} = 0.08$

.

measurement technique which is the subject of the next section.

3.3 Interferometric Transmission-based Near-field Scanning Optical Microscopy: i-TraNSOM

3.3.1 Introduction

As mentioned in the introduction to this chapter, techniques for characterizing optical modes are limited in resolution or collection efficiency rendering them incapable of characterizing optical modes with sub-100 nm optical features. In the previous section we have introduced a new TraNSOM technique aimed at solving this problem. While this technique works well for measuring the polarization component of light parallel to the probe axis, other polarization components are inefficiently characterized. Since in this dissertation we are interested in highly confined modes which are confined to nanoscale dielectric slots, we require measurement of polarization components perpendicular to the probe axis.

To overcome the limitations of current near field measurement techniques and directly measure sub-100 nm light confinement in a dielectric slot, we measure the phase shift of the optical mode induced by a scanning nanoscale Atomic Force Microscope (AFM) probe. Unlike current apertureless NSOM techniques (including the TraNSOM technique discussed in the previous chapter [14, 4]), by detecting the phase shift induced by the probe we ensure that the measurement is polarization independent [24]. This is allows us to directly measure the highly confined slot mode which has a large in-plane polarization component.

To measure the phase shift induced by the probe we implement the TraNSOM apparatus in an interferometer and thus we call this phase sensitive near

field measurement technique interferometric Transmission-based Near field Scanning Optical Microscopy or i-TraNSOM.

3.3.2 Experimental Setup

The experimental setup is nearly identical to that described in Section 3.2.2 with two important differences. First, the probe used in this experiment is a high aspect ratio silicon probe shown in Fig. 3.5(d). Since here are interested using the probe to induce a phase shift as opposed to create loss we use a dielectric probe with a known index of refraction as opposed to a highly-scattering metallic probe as was used in Section 3.2. Second, the slot waveguide is placed in an unbalanced Mach-Zender Interferometer (MZI) since since this allows us to measure the phase shift induced in the slot waveguide by monitoring the power transmitted through the MZI.

A scanning electron micrograph (SEM) of the slot waveguide structure measured in this section is shown in Fig. 3.5(a). Figure 3.5(b) plots for the fundamental TE mode showing confinement of light to the slot region as calculated with a finite element mode solver.

The MZI used in this experiment (Fig. 3.5(d)) was fabricated in 250 nm thick silicon on insulator using electron beam lithography and reactive ion etching. The device is approximately 250 microns long consisting of one arm with a 300 nm wide reference waveguide, and another arm with a 450 nm wide waveguide with an 85 nm slot (measured at the waveguide center via SEM). Coupling between the arms is achieved using directional couplers. To measure the change in phase velocity induced by the probe we record the power transmitted through

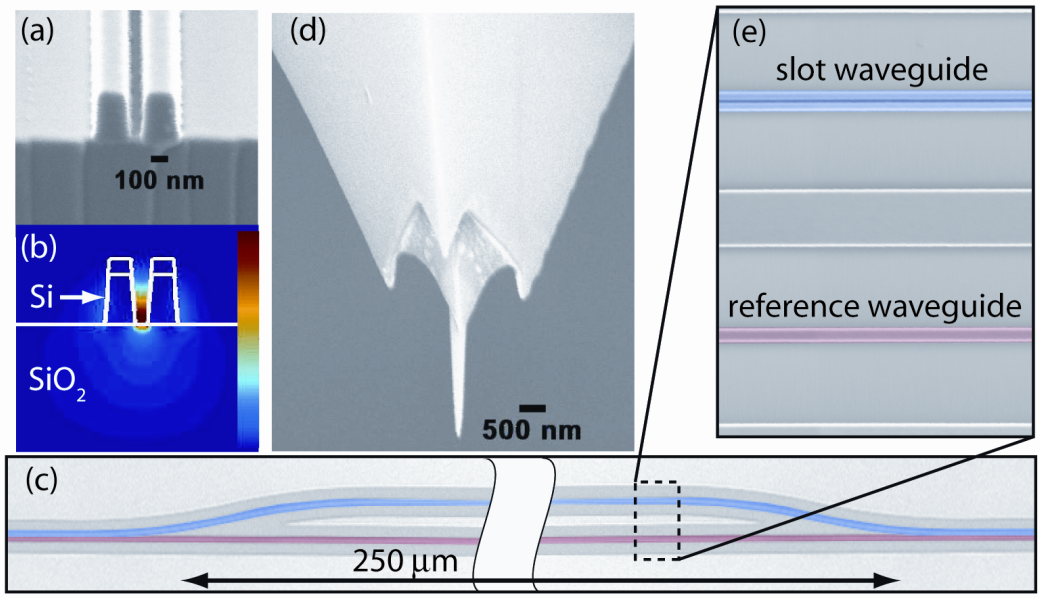

Figure 3.5: (a) SEM image of the silicon slot waveguide cross section. (b) $|E|^2$ for the fundamental TE mode of the slot waveguide. (c) SEM image of the unbalanced Mach-Zender interferometer showing the slot waveguide and reference waveguide in false color. (d) SEM image of the silicon AFM probe (e) SEM image showing the slot (top) and reference (bottom) waveguides in false color.

the MZI as we scan the slot waveguide with the silicon probe. Since the effective refractive index of each arm is different, we can tune the phase relationship between the reference and slot arm by tuning the input wavelength. Details of the fabrication process are discussed in Section 3.2.4.

3.3.3 Measurement of Light Confinement in Nanoscale Slot Waveguides

To measure the field confined to the 85 nm slot region shown in Fig. 3.5 we record the power as we scan the slot waveguide with an AFM probe. The

change in transmission (ΔT) through the MZI is directly proportional to the local electric field intensity ($|E|^2$). This can be understood by noting that at a wavelength in which the two arms are out of phase, the transmission is proportional to $\cos(-\pi/2+\delta)$ or $\sin(\delta)$ where $\delta = \pm 2\pi\Delta n_{eff}L/\lambda$ is the phase difference induced by the probe and L is the interaction length with the probe. Δn_{eff} is the increase in the effective index due to the interaction with the probe which to first order can be written as [24, 25]:

$$\Delta n_{eff} = \frac{n_p}{n_{eff}} \cdot \frac{\int_{A_p} |\mathbf{E}|^2 da}{\int_{\infty} |\mathbf{E}|^2 da} \tag{3.7}$$

where n_p and A_p are the refractive index and cross-sectional area of the probe respectively. In our configuration $\Delta n_{eff} < 1$ and $L \approx \lambda/15$; therefore, we expect a maximum probe-induced phase shift of $|\delta| < \pi/8$ radians. Using the small angle approximation the change in transmission is therefore given by:

$$\Delta T \propto \sin(\delta) \approx \delta \propto \int_{A_p} |\mathbf{E}|^2 da. \tag{3.8}$$

The measured topography of the slot waveguide and simultaneously recorded transmitted power are shown in Fig. 3.6(a) and (b) respectively. The large increase in transmission when the probe is in the slot is a direct measurement of the strong electric field confined in this region. The solid line in Fig. 3.6(c) shows a cross section of the TraNSOM measurement. Notice the sharp peak of the field in the slot has 20 nm full width half-maximum which agrees with the simulated phase shift (dashed line) computed by convolving the probe profile with the fundamental TE mode shown in Fig. 3.5(b). We chose a wavelength of 1524.5 nm for this measurement since this corresponds to a phase dif-

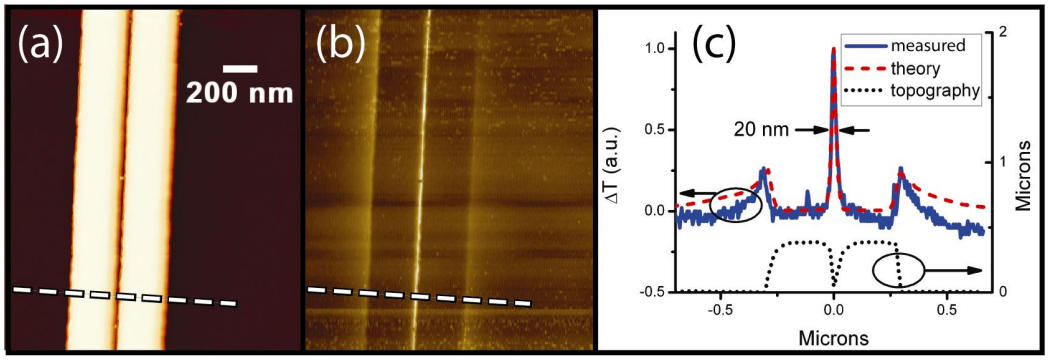

Figure 3.6: (a) AFM topography of the slot waveguide. (b) simultaneously recorded transmission through the MZI shown in Fig. 3.5((c). (c) solid line: cross section through the dashed line in (b); dotted line: simultaneously recorded waveguide topography; dashed line: simulated convolution of the probe profile with $|\mathbf{E}|^2$ of the fundamental slot mode shown in Fig. 3.5(b).

ference of $\delta\phi = -\pi/2$ between the two arms of the MZI where $\Delta\phi \equiv \phi_s - \phi_r$ and ϕ_s and ϕ_r are the phase accumulated in the slot and reference waveguide respectively. This is marked as λ_1 in Fig. 3.7(a) where we plot the transmission through the MZI as a function of wavelength. Since the reference waveguide has a larger effective index and thus longer optical path length, λ_1 corresponds to the case where the reference waveguide has acquired an additional phase of $\pi/2$ compared to the slot waveguide ($\Delta\phi = -\pi/2$).

To confirm that we are measuring changes in phase velocity we record the power transmitted through the MZI as we scan the reference and slot waveguides at different wavelengths. As mentioned above $\lambda_1 = 1524.75$ nm in Fig. 3.7(a) corresponds to $\Delta\phi = -\pi/2$. Since the probe always increases the phase acquired in the arm being scanned, according to our definition of $\Delta\phi$, we expect the additional phase difference induced by the probe (δ defined above) to be positive when scanning the slot waveguide and negative when scanning the reference waveguide. Since at this wavelength ΔT is proportional to δ, we

expect the transmission to increase when scanning the slot waveguide and decrease when scanning the reference waveguide. Figure 3.7(c) and (d) show the change in transmitted power (ΔT) as a function of probe position in the slot waveguide and in the reference waveguide respectively. To compare the sign of ΔT between images we have normalized each figure to $|\Delta T|$. One can see that as expected, at λ_1, scanning the slot waveguide increases the transmission through the MZI while scanning the reference waveguide decreases the transmitted power. Changing the wavelength to $\lambda = 1526.5$ nm in Fig. 3.7(a) we change to a situation where the reference waveguide has acquired an extra phase of $3\pi/2$ compared to the slot waveguide ($\Delta\phi = -\pi/2$). In this case $\Delta T \propto -\sin(\delta) \approx \delta$. Therefore we expect the transmission to *decrease* when scanning the slot waveguide and *increase* when scanning the reference waveguide. Figure 3.7(d) and (e) show the transmitted power as a function of probe position for the slot and reference waveguide respectively. As expected, the sign of ΔT has changed as a result of changing the wavelength to λ_2. This confirms that we are indeed measuring the effect of the probe on the phase velocity, and this effect dominates over other effects such as induced loss due to scattering. Note that if the dominant effect was probe-induced scattering, we would expect the transmitted power to decrease at *both* λ_1 *and* λ_2 as we scan the waveguide propagating the most power.

3.3.4 Summary

In this section we have introduced a new high-resolution polarization-insensitive optical measurement technique. Using this technique we were able to make the first direct measurement of light confinement below $\lambda/2n$ in di-

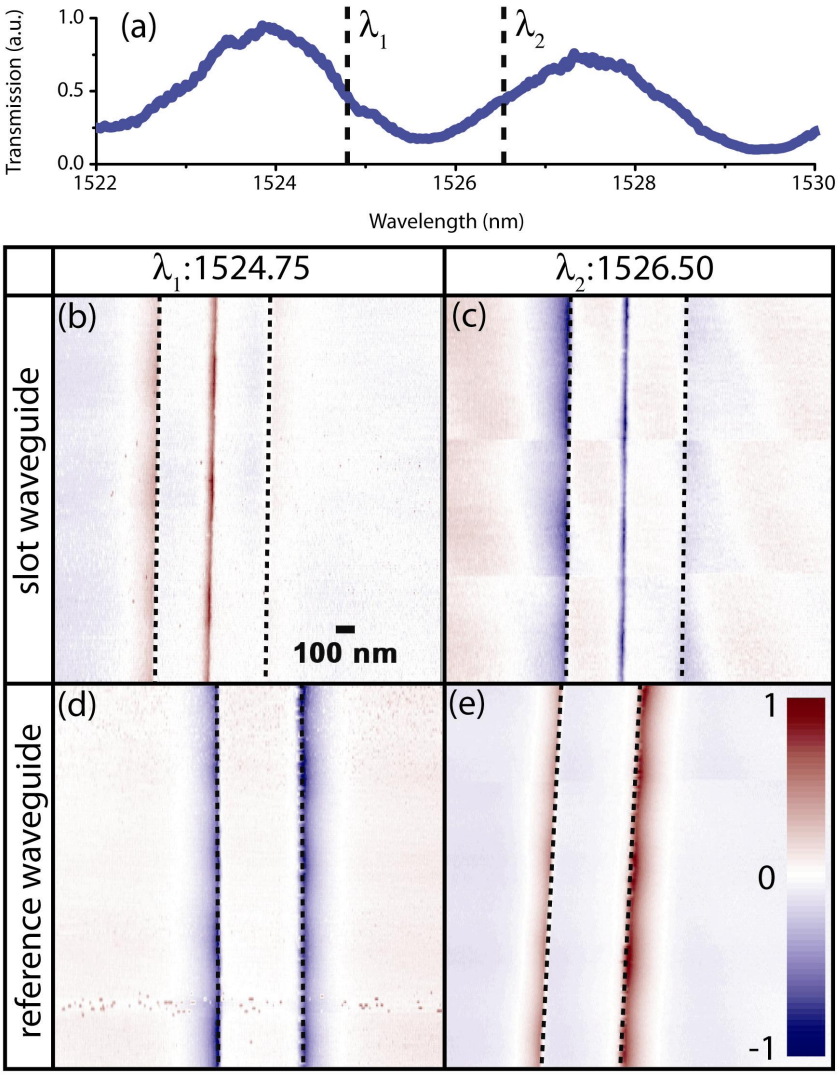

Figure 3.7: Transmitted power through the MZI as a function of wavelength. (b) and (c): Normalized change in transmission through the MZI as the slot waveguide is scanned with $\lambda = 1524.75$ nm and $\lambda = 1526.50$ nm respectively. (d) and (e): Normalized change in transmission through the MZI as the reference waveguide is scanned with $lambda = 1524.75$ nm and $\lambda = 1526.50$ nm respectively.

electric materials. This underscores the point that the degree of light confinement possible in transparent media is not fundamentally limited by the wavelength. Additionally, the dielectric materials used here have extremely low optical losses allowing long propagation lengths and high quality factor resonant cavities. Devices based on this strong light confinement in dielectrics will find applications in a number of areas which benefit from increased light-matter interaction.

3.4 Summary

In this chapter we have discussed two new near field measurement techniques: TraNSOM and i-TraNSOM. The main advantage of these techniques is that they offer superior resolution compared to standard NSOM techniques and can be easily implemented on commercial AFM systems.

We have shown the TraNSOM technique like other scattering-based NSOM techniques is highly polarization sensitive and selects primarily the polarization component along the long axis of the probe. We have used this technique to measure optical features smaller than $\lambda/15$ in the near-IR. By carefully analyzing the signal collected during the TraNSOM measurements we were able to quantify the scattering efficiency of the probe for different polarizations. This could become a powerful technique to characterize the scattering properties of nanoscale objects.

As opposed to scattering-based NSOM techniques (including the TraNSOM) we have shown that the i-TraNSOM measures all polarizations equally. This is critically important for characterizing the interaction between light and mat-

ter at the nanoscale particularly in slot waveguides. With this technique we have presented the first direct experimental measurement of light confinement to sub-$\lambda/2$ dimensions in dielectric materials.

The nanoscale light confinement presented in Chapter 2 and measured in this chapter can have important ramifications for the efficiency of devices based on light-matter interaction. Some representative applications will be discussed in the next chapter.

BIBLIOGRAPHY

[1] R. Naisheng, R. Jones, L. Ansheng, O. Cohen, D. Hak, A. Fang, and M. Paniccia, "A continuous-wave Raman silicon laser," Nature **433,** 725–8 (2005).

[2] I. Stefanon, S. Blaize, A. Bruyant, S. Aubert, G. Lerondel, R. Bachelot, and P. Royer, "Heterodyne detection of guided waves using a scattering-type scanning near-field optical microscope," Opt. Express 13 (2005).

[3] M. L. M. Balistreri, H. Gersen, J. P. Korterik, L. Kuipers, and N. F. van Hulst, "Tracking Femtosecond Laser Pulses in Space and Time," Science **294,** 1080–1082 (2001).

[4] W. C. L. Hopman, K. O. v. d. Werf, A. J. F. Hollink, W. Bogaerts, V. Subramaniam, and R. M. d. Ridder, "Nano-mechanical tuning and imaging of a photonic crystal micro-cavity resonance," Opt. Express **14,** 8745–8752 (2006).

[5] S. Bourzeix, J. M. Moison, A. F. Mignard, F. Barthe, A. C. Boccara, C. Licoppe, B. Mersali, M. Allovon, and A. Bruno, "Near-field optical imaging of light propagation in semiconductor waveguide structures," Appl. Phys. Lett. **73,** 1035–7 (1998).

[6] B. Hecht, B. Sick, U. P. Wild, V. Deckert, R. Zenobi, O. J. F. Martin, and D. W. Pohl, "Scanning near-field optical microscopy with aperture probes: Fundamentals and applications," J. Chem. Phys. **112,** 7761–74 (2000).

[7] C. D. Poweleit, D. H. Naghski, S. M. Lindsay, J. T. Boyd, and H. E. Jackson, "Near field scanning optical microscopy measurements of optical intensity distributions in semiconductor channel waveguides," Appl. Phys. Lett. **69,** 3471–3 (1996).

[8] G. H. Vander Rhodes, B. B. Goldberg, M. S. Unlu, S. T. Chu, W. Pan, T. Kaneko, Y. Kokobun, and B. E. Little, "Measurement of internal spatial modes and local propagation properties in optical waveguides," Appl. Phys. Lett. **75,** 2368–70 (1999).

[9] H. A. Bethe, "Theory of Diffraction by Small Holes," Phys. Rev. **66,** 163 (1944).

[10] R. Bachelot, P. Gleyzes, and A. C. Boccara, "Near-field optical microscope

based on local perturbation of a diffraction spot," Opt. Lett. **20,** 1924–6 (1995).

[11] Y. Inouye and S. Kawata, "Near-field scanning optical microscope with a metallic probe tip," Opt. Lett. **19,** 159–61 (1994).

[12] R. Bachelot, G. Lerondel, S. Blaize, S. Aubert, A. Bruyant, and P. Royer, "Probing photonic and optoelectronic structures by Apertureless Scanning Near-Field Optical Microscopy," Microscopy Research and Technique **64,** 441–452 (2004).

[13] L. Gomez *et al.*, "Apertureless scanning near-field optical microscopy: a comparison between homodyne and heterodyne approaches," J. Opt. Soc. Am. B **23,** 823–33 (2006).

[14] J. T. Robinson, S. F. Preble, and M. Lipson, "Imaging highly confined modes in sub-micron scale silicon waveguides using transmission-based near-field scanning optical microscopy," Opt. Express **14,** 10588–10595 (2006).

[15] A. F. Koenderink, M. Kafesaki, B. C. Buchler, and V. Sandoghdar, "Controlling the resonance of a photonic crystal microcavity by a near-field probe," Phys. Rev. Lett. **95,** 153904–1 (2005).

[16] L. Aigony, A. Lahrech, S. Gresillon, H. Cory, A. C. Boccara, and J. C. Rivoal, "Polarization effects in apertureless scanning near-field optical microscopy: an experimental study," Opt. Lett. **24,** 187–9 (1999).

[17] M. Labardi, M. Allegrini, M. Zavelani-Rossi, D. Polli, G. Cerullo, S. De Silvestri, and O. Svelto, "Highly efficient second-harmonic nanosource for near-field optics and microscopy," Opt. Lett. **29,** 62–4 (2004).

[18] W. Hopman, R. Stoffer, and R. de Ridder, "High-Resolution Measurement of Resonant Wave Patterns by Perturbing the Evanescent Field Using a Nanosized Probe in a Transmission Scanning Near-Field Optical Microscopy Configuration," J. Lightwave Technol. **25,** 1811–1818 (2007).

[19] L. Lalouat, B. Cluzel, F. de Fornel, P. Velha, P. Lalanne, D. Peyrade, E. Picard, T. Charvolin, and E. Hadji, "Subwavelength imaging of light confinement in high-Q/small-V photonic crystal nanocavity," Appl. Phys. Lett. **92,** 111111–3 (2008).

[20] S. J. McNab, N. Moll, and Y. A. Vlasov, "Ultra-low loss photonic integrated

circuit with membrane-type photonic crystal waveguides," Opt. Express 11 (2003).

[21] J. D. Jackson, *Classical electrodynamics*, 3rd ed. (John Wiley & Sons, Inc., Hoboken, NJ, 1999).

[22] H. Van de Hulst, *Light scattering by small particles* (Dover Publications. Inc., New York, NY, 1981).

[23] V. R. Almeida, R. R. Panepucci, and M. Lipson, "Nanotaper for compact mode conversion," Opt. Lett. **28,** 1302–4 (2003).

[24] I. Marki, M. Salt, and H. P. Herzig, "Tuning the resonance of a photonic crystal microcavity with an AFM probe," Opt. Express **14,** 2969–2978 (2006).

[25] L. A. Coldren and S. W. Corzine, *Diode Lasers and Photonic Integrated Circuits* (J. Wiley & Sons, New York, NY, 1995).

CHAPTER 4

APPLICATIONS OF NANOSCALE LIGHT CONFINEMENT

4.1 Introduction

As discussed in Chapter 1 decreasing the size of photonic devices can improve their efficiency by enhancing the interaction between light and matter. In this chapter we analyze two applications which benefit from enhanced light-matter interaction.

In Section 4.2 we analyze the use of nanoscale slot waveguides to achieve gain and lasing in a silicon-based device. We show that new figures of merit need to be considered when optimizing these structures for lasing applications. Namely we show why the power confined to the slot region is not a useful metric. Using the appropriate metrics we show that slot-based devices can perform surprisingly well for lasing applications than would be expected based on power confinement.

In Section 4.3 we demonstrate a highly sensitive on-chip refractometric gas sensor based on slotted resonant cavities. We analyze the sensitivity of this device and use it to measure acetylene gas at varying pressures. At the time of this dissertation this remains the most sensitive refractometric silicon photonic gas sensor[1].

[1]Portions of this chapter are reproduced with permission from [1] and [2]

4.2 Optical Gain in Slot Waveguides

4.2.1 Introduction

A critical photonic component yet to be demonstrated on a silicon-based platform is an electrically pumped device with optical gain for amplification or lasing. Achieving this optical gain in a silicon-based device is extremely challenging since silicon is an indirect band-gap semiconductor and therefore an inefficient photon source. Hybrid silicon devices based on direct band-gap III-V materials bonded to silicon photonic elements present an interim solution [3], however, the reliance on a wafer bonding step prohibits a high throughput fabrication process possible with a silicon-based process.

One possible configuration for silicon-based gain is the recently proposed slot waveguide design [4, 5]. In this configuration a low-index gain material such as Er-doped SiO_2 or Er-doped Si_3N_4 can be inserted into one [6] or multiple [7, 8] thin slots between two silicon rails (see Fig. 4.1(a)). Electrical excitation of the gain material could be achieved by passing a tunneling current through the slot-region.

One key advantage of this configuration is the large optical field enhancement in the slot-region due to the boundary conditions imposed on the electric field normal the slot interface (see Chapter 2). Since the normal electric displacement ($D = \epsilon E$) must be continuous across the interface, the electric field in the slot waveguide is enhanced by the ratio of the dielectric constant of silicon to that of the slot material. In semiconductor materials this enhancement can be as large as one order of magnitude.

In the following sections we derive from first principles the appropriate confinement factors and figures of merit for modal gain in high-index-contrast waveguides. We show explicitly that the modal gain is dependent on two quantities: the group velocity and the electric field energy confinement in the slot region. The lasing threshold however is independent of the group velocity (for a cavity with negligible end-mirror losses) and determined only by the electric field energy confinement. We also show that in some instances decreasing the width of the slot can decrease the lasing threshold despite the reduction of gain material. This counter-intuitive result can be understood as the increased emission rate for material in narrow slots [9] overcoming the reduction in volume of gain material. Additionally we show that the percentage of power confined to the slot region (sometimes used as a confinement factor) can incorrectly predict the modal gain in high-index-contrast waveguides.

4.2.2 Why Power Confinement is Unimportant

Typically waveguide gain is assumed to be proportional to the percentage of the guided mode power which overlaps with the gain medium; however, this is not true for high-index contrast waveguides due to the large electric field discontinuities at dielectric interfaces. This discrepancy results from Fermi's Golden Rule which states that the electric field of an electromagnetic wave, not the power, determines the emission rate for an excited state and consequently the modal gain (see Section 2.2 and [10]).

In standard low-index-contrast waveguides, optical gain and power confinement are considered proportional based on the following arguments. For elec-

tromagnetic plane waves in homogenous media the magnetic field **H** can be written in terms of the electric field **E** and the impedance of the material according to:

$$\mathbf{H} = \frac{c\epsilon}{n}(\hat{\mathbf{e}}_z \times \mathbf{E}) \tag{4.1}$$

where $\hat{\mathbf{e}}_z$ is a unit vector along the direction of propagation (which we have chosen to be the z-direction) and n is the index of refraction of the material. This is often written in the form relating the major components of the electric and magnetic fields (for a TM mode in this case):

$$E_y = \frac{-\omega\mu_0}{\beta}H_x, \tag{4.2}$$

where β is the propagation constant defined as $\beta \equiv 2\pi\overline{n}/\lambda$ (and $\overline{n}$ is the effective refractive index of the guided mode) [4]. Based on these relationships the electric field energy, and waveguide power stored in a given region can be used interchangeably since they differ only be a constant. In this case the percentage of power overlapping the gain medium can be used to calculate the resulting modal gain, and it is often assumed that the same is true for high-index contrast structures.

For high-index-contrast waveguides, however, the linear relationships between the electric and magnetic fields (Eqs. 4.1 and 4.2) do not hold since they must satisfy different boundary conditions. This is shown in Fig. 4.1. For low-index-contrast waveguides, Eqs. 4.1 and 4.2 are close approximations. Figure 4.1 (a) and (b) shows the fundamental TM modewith an index difference of 0.25 between the core and cladding. We see close agreement in the magnitude and spatial profiles of these two fields. However, as the index-contrast is increased to 2.5 (Fig. 4.1(c) and (d)) there is a noticeable difference between E_y and $\frac{-\omega\mu_0}{\beta}H_x$. Notice that E_y must be *continuous* across the dielectric inter-

faces to the left and right of the waveguide, and *discontinuous* across the top and bottom interfaces. On the other hand, Hx must be continuous across all interfaces since the magnetic susceptibility is the same in all regions. This leads to noticeable differences between the electric and magnetic field magnitudes and profiles. This difference becomes dramatic when the peak of the electric field is placed at a dielectric discontinuity as is the case for slot waveguides (Fig. 4.1(e) and (f)).

The strong difference between the spatial distribution of the electric and magnetic fields in high index contrast is the reason that power confinement is no longer a relevant quantity when calculating gain in high-index-contrast waveguides. This issue is also present when calculating the sensitivity of waveguides to changes in refractive index. Several previous papers have overcome this problem by either determining waveguide sensitivity empirically [11] or by introducing correction factors [12], however, there is little discussion as to the origin of the correction factors.

In the next section we will formulate from first principles the correct figures of merit for gain in high-index contrast waveguides.

4.2.3 Confinement Factor for Slot Waveguides

To rigorously calculate gain in high-index-contrast waveguides we derive from first principles. a proportionality constant (known as a confinement factor Γ) which relates bulk material gain (g_m) to the modal gain (g_m) in a guiding structure:

$$\Gamma \equiv g_m / g_b, \tag{4.3}$$

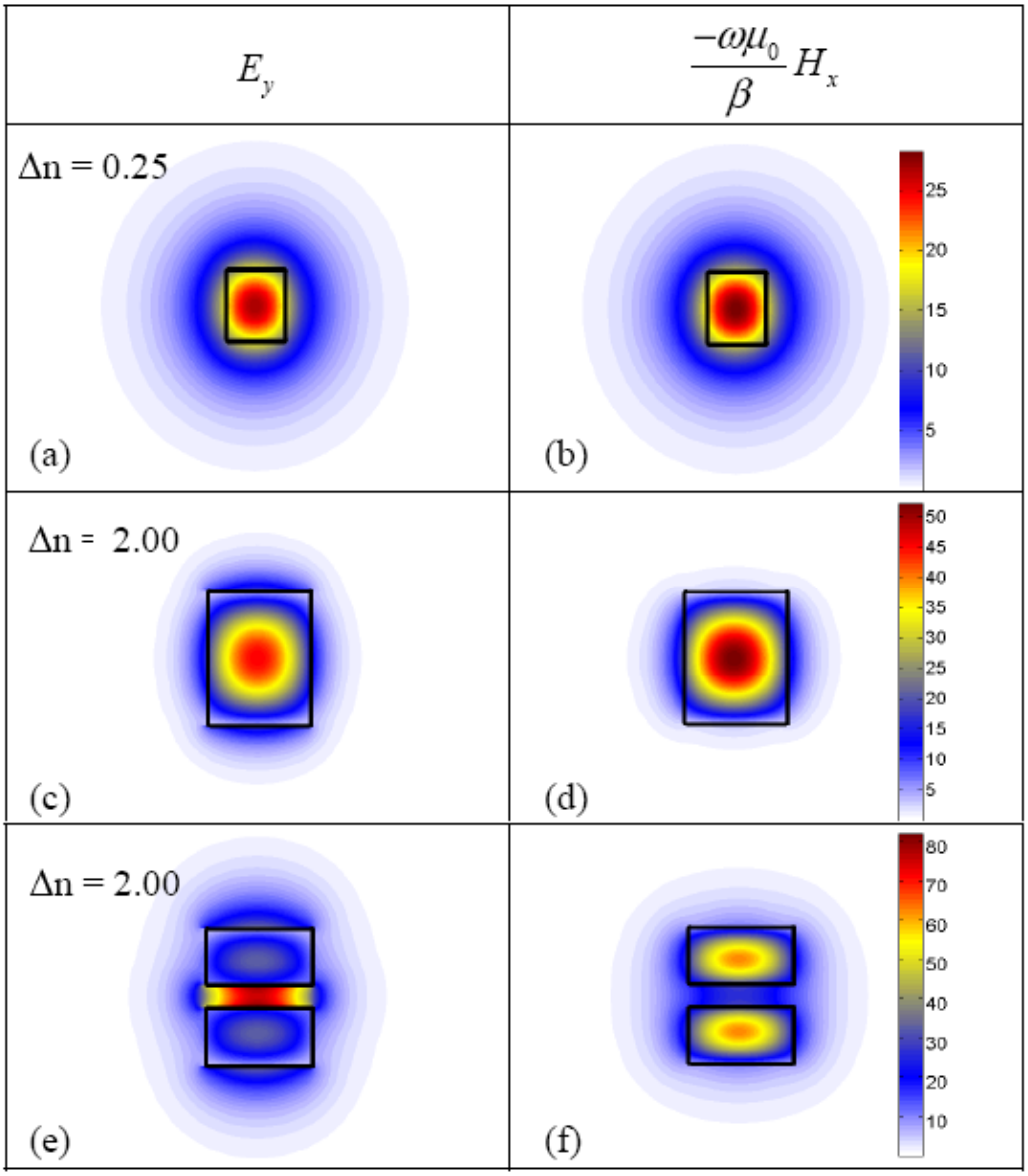

Figure 4.1: Fundamental TM modes at a wavelength of 1.5 μm for waveguides 500 nm wide and 600 nm tall. All modes are normalized to unit power. The high-index material ($n = 3.5$) is outlined in black. The waveguides are clad with $n = 3.25$ for (a) and (b) and $n = 1.5$ for (c)-(f). The first and second columns show E_y and $\frac{-\omega\mu_0}{\beta} H_x$ respectively, plotted on the same color scale. The two fields become increasingly dissimilar as more electric field is concentrated at high-index-contrast boundaries.

where and have units of inverse length. (Note that Γ here refers to the confinement factor and not the spontaneous emission rate as in Section 2.2.) Although a similar derivation has been shown in [13] we develop a simplified expression and include our derivation for pedagogical reasons. The bulk material gain can be determined from the magnitude of the electric field for a plane wave propagating along the z-direction through the gain medium:

$$|E(z)|^2 = |E_0|^2 e^{g_b z}. \tag{4.4}$$

To calculate the effective confinement factor for a given waveguide mode profile, we begin with an expression for the electric field of a guided mode propagating along the z-direction. This can be written as the sum of all three vector components of the electric field using Einstein summation notation:

$$\mathbf{E}(x, y, z) = \hat{\mathbf{e}}_j E_{j0} \Psi(x, y)_j e^{i(\omega t - \tilde{\beta} z)}, \tag{4.5}$$

where ê is the polarization unit vector,Ψ is the cross sectional mode profile, and $\tilde{\beta}$ is the complex propagation constant defined as

$$\tilde{\beta} \equiv k_0(\overline{n}_r + i\overline{n}_i), \tag{4.6}$$

where k_0 is the angular wavenumber in free space, and $\overline{n}_r$ and $\overline{n}_i$ are the real and imaginary parts of the effective index respectively. By writing Eq. 4.5 in the same form as Eq. 4.4 we can see that the modal gain is determined by the complex propagation constant. From Eq. 4.6 we can then write the gain of the guided mode in terms of the imaginary part of the effective index:

$$g_m = 2\text{Im}\{\tilde{\beta}\} = 2k_0\overline{n}_i. \tag{4.7}$$

Similarly we can write the bulk material gain in terms of the imaginary part of refractive index of the active gain material:

$$g_b = 2k_0 n_{Ai}. \tag{4.8}$$

Expressing gain in this form allows us to treat it as a perturbation to the refractive index of the waveguide. We can now calculate the modal gain by introducing a small imaginary part to the refractive index (Δn_{Ai}) in a given active region (A) and solve for the complex propagation constant of the guided mode. This can be performed using variational methods [14]:

$$\Delta\tilde{\beta} = \frac{\omega \int\int_{\infty} \Delta\tilde{\epsilon}|\mathbf{E}|^2 dxdy}{\frac{1}{2}\int\int_{\infty} \text{Re}\{\ \mathbf{E}\times\mathbf{H}^*\ \}\ \cdot\hat{\mathbf{e}}_z dxdy} \tag{4.9}$$

where $\Delta\tilde{\epsilon} = (n_A + i\Delta n_{Ai})^2$. According to Eqs. 4.6-4.8 this can be written in the form:

$$g_m = \left[\frac{n_A c\epsilon_0 \int\int_A |\mathbf{E}|^2 dxdy}{\int\int_{\infty} \text{Re}\{\mathbf{E}\times\mathbf{H}^*\}\cdot\hat{\mathbf{e}}_z dxdy}\right] g_b \tag{4.10}$$

Here c is the speed of light in vacuum, the integral in the numerator is carried out only over the area of the active gain region (since this is where $\Delta\tilde{epsilon} \neq 0$), and the integral in the denominator is carried out over the entire cross section of the mode. We recognize the term in the brackets as the proportionality constant in Eq. 4.3 and therefore we can express the confinement factor as:

$$\Gamma = \frac{n_A c\epsilon_0 \int\int_A |\mathbf{E}|^2 dxdy}{\int\int_{\infty} \text{Re}\{\mathbf{E}\times\mathbf{H}^*\}\cdot\hat{\mathbf{e}}_z dxdy} \tag{4.11}$$

Note that as expected the stimulated emission rate (and thus the gain), depends on the intensity of the field which is proportional to $|\mathbf{E}|^2$. Since this term is normalized to unit power, the confinement factor can be thought of as the amount of intensity overlapping the gain medium per unit input power. Note that most previous derivations of this confinement factor err by incorrectly substituting the electric for magnetic field in attempts to simplify the expression. This is commonly written as [15, 16, 17]:

$$\frac{1}{2}\int\int \text{Re}\{\mathbf{E}\times\mathbf{H}^*\}\cdot\hat{\mathbf{e}}_z dxdy = \frac{1}{2}\frac{\beta}{\omega\mu_0}\int\int |\mathbf{E}|^2 dxdy, \tag{4.12}$$

and thus Eq. 4.11 could be written as the percentage of power or intensity confined to the active region. However, as shown in Section 4.2.2, ***the expression in***

Eq. 4.12 is not valid for high-index-contrast waveguides since it is based on the relationship for plane waves in homogeneous media that $\mathbf{H} = \frac{\epsilon c}{\bar{n}}(\hat{\mathbf{e}}_z \times \mathbf{E})$[18].

The expression for the confinement factor (Eq. 4.9) can be simplified into the product of two terms: one related to the group velocity, and the other related to the confinement of the energy density of the electric field. The energy stored per unit length (U/l) in a dielectric waveguide can be written as [18]:

$$U/l = \frac{1}{2}\int\int_{\infty} \epsilon|\mathbf{E}|^2 dxdy. \tag{4.13}$$

Note that here we have neglected material dispersion when writing the stored energy per unit length. To account for material dispersion one should replace epsilon with $d(\omega\epsilon)/d\omega$ in Eq. 4.13 [19, 20]. If silicon is the most dispersive material, the error introduced by making this approximation is less than 7% at a wavelength of 1.55 microns. The group velocity of the mode (v_g) describes the speed with which energy flows through a given cross section. Therefore we can write the power flux through a given cross section of the waveguide as:

$$\frac{1}{2}\int\int \mathrm{Re}\left\{\mathbf{E}\times\mathbf{H}^*\right\}\cdot\hat{\mathbf{e}}_z dxdy = v_g\frac{1}{2}\int\int \epsilon|\mathbf{E}|^2 dxdy. \tag{4.14}$$

Using the definition of group index ($n_g \equiv c/v_g$) we substitute Eq. 4.14 into Eq. 4.11 and rewrite the confinement factor as:

$$\Gamma = \frac{n_g}{n_A}\frac{\int\int_A \epsilon|\mathbf{E}|^2 dxdy}{\int\int_{\infty} \epsilon|\mathbf{E}|^2 dxdy} \equiv \frac{n_g}{n_A}\gamma_A. \tag{4.15}$$

We see from the simplified expression for the confinement factor that the modal gain can be defined as the product of a term related to the group index and a term related to the confinement of the electric field energy density. The first term can be thought of as a confinement in time since increasing the real part of the group index relative to the bulk index has the effect of slowing

the propagation of the guided mode. Therefore for a given waveguide length, light can spend more time in the gain media resulting in an enhancement of the modal gain per unit length. The second term represents the spatial confinement of the energy density to the active region of the waveguide which we define as:

$$\gamma_A \equiv \frac{\int\int_A \epsilon|\mathbf{E}|^2 dxdy}{\int\int_\infty \epsilon|\mathbf{E}|^2 dxdy}. \tag{4.16}$$

Since this term can be as large as 1 we see that the total confinement factor in Eq. 4.15 can be larger than 1 if the group index is larger than the bulk refractive index. This means that it is possible to achieve more gain per unit length in a guided structure than would be possible in bulk. This phenomenon has been noted before for modal absorption [21] and results from the fact that light spends more time in a structure with a large group index, and thus interacts more with the gain material per unit length.

4.2.4 Numerical Verification

To verify our expression for the confinement factor (Eq. 4.13) we use numerical methods to calculate the relationship between material gain and modal gain and compare it to the analytical results. Since the material gain can be expressed in terms of an imaginary part of the dielectric constant, we can simulate material gain in a given waveguide region by adding an imaginary component to the dielectric constant and calculating the propagation constant of the guided mode using a finite difference mode solver. The imaginary part of this complex propagation constant can then be written in terms of the modal gain according to Eq. 4.7. This relationship between the modal gain and material gain is the definition of the confinement factor Eq. 4.3 and should match the derived expression Eq. 4.15.

We numerically calculate the modal gain according to the waveguide geometry and the corresponding fundamental TM mode as shown in Fig. 4.2(a) and (b) respectively. The waveguide geometry consists of two high index rails 500 nm wide and 250 nm tall separated by a horizontal slot 50 nm tall. For simplicity we use a wavelength of 1.5 μm and 3.5 and 1.5 for the high and low refractive indices respectively. This is approximately the index contrast between Si and SiO_2. Figure 4.2(b) shows the fundamental TM mode calculated using a Matlab-based finite difference mode solver. We simulate material gain by introducing an imaginary part of the dielectric constant to the low-index slot region. For each value of material gain we use the finite difference mode solver to calculate the complex propagation constant and calculate the corresponding modal gain according to Eq. 4.7.

By plotting the numerically calculated modal gain (g_m) versus material gain (g_b) in Fig. 1(c) we show excellent agreement with the analytically calculated confinement factor. The slope of the line g_m versus g_b (circles in Fig. 4.1(c)) represents the confinement factor according to Eq. 4.3. We also calculate the confinement factor based on Eq. 4.15 and the calculated TM mode in Fig. 4.1(b). We plot Γg_b as the dashed line in Fig. 4.1(c). As expected, our calculated confinement factor agrees very well with the relationship between the modal and material gain from numerical simulations. The difference between these two factors (0.4328 from Eq. 4.15) and 0.4368 from the numerical simulations) is less than 1%. To highlight the difference between this confinement factor and the confinement of power to the gain medium we also plot on this graph P_A where we define the power in the active region as:

$$P_A \equiv frac \int\int_A \mathrm{Re}\left\{\mathbf{E}\times\mathbf{H}^*\right\}\cdot\hat{\mathbf{e}}_z dxdy \int\int_\infty \mathrm{Re}\left\{\mathbf{E}\times\mathbf{H}^*\right\}\cdot\hat{\mathbf{e}}_z dxdy. \qquad (4.17)$$

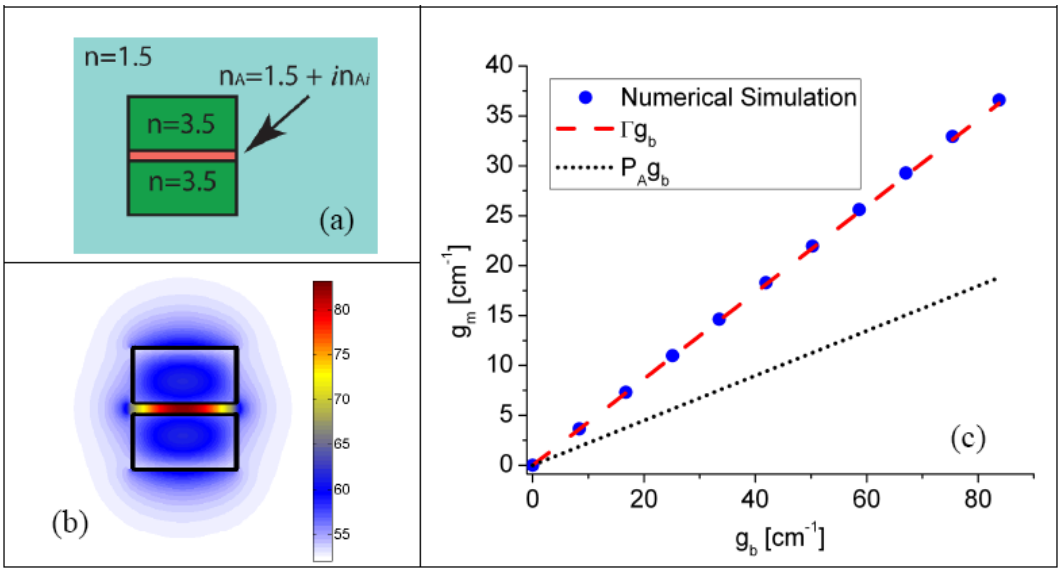

Figure 4.2: Numerical study of modal gain. (a) Schematic of slot waveguide with gain material defined by an imaginary component of the refractive index confined to the slot region (pink). (b) Major field component of the fundamental TM mode for the same structure as (a) calculated using a finite difference mode solver. (c) Circles show the modal gain (g_m) calculated from the complex effective index of the fundamental TM mode as determined using a finite difference mode solver. Material gain is added via the imaginary part of the refractive index in the slot. Dashed line shows the modal gain calculated according to Eq. 4.3 based on the confinement factor Γ determined from the zero-gain mode profile from Eq. 4.15. Dotted line shows the product of the power in the active gain region (P_A) and the material gain. We see that the confinement factor proposed in this paper correctly predicts the modal gain simulated numerically, while the power confinement greatly underestimates the simulated modal gain.

We see from Fig. 4.1(c) that the modal gain of a slot waveguide is substantially larger than would be expected from the percentage of power confined to the gain region. As discussed in Section 4.2.3, this enhanced modal gain results from both the large group index as well as the increased electric field energy density in the slot. The electric field energy density is underestimated using the **H** field (See Fig. 4.1(e) and (f)).

4.2.5 Minimizing the Lasing Threshold

One of the primary interests in these structures is achieving lasing, therefore it is important to identify which factors aid in reaching the condition that the modal gain exceeds the modal loss. Since material gain was written as a positive imaginary part of the material's refractive index, similarly, material loss can be written as a negative imaginary part of the refractive index. The modal loss can then be determined following the same derivation in Section 4.2.3. The result is the modal loss (α_m) is related to the bulk material loss (α_b) by

$$\alpha_m = \frac{n_g}{n_b}\gamma_b\alpha_b, \tag{4.18}$$

where n_b is the refractive index of the bulk material and γ_b is the electric field energy density confinement in the material similar to Eq. 4.16. In general there will be several loss mechanisms which can be written as sum of terms of the form Eq. 4.18. We do not consider here non-distributed losses, such as end-mirror loss, which are not fundamentally limiting to a waveguide structure (through the application of high-reflection mirror coatings and/or lengthening of the laser cavity). To achieve lasing, the threshold condition requires the modal gain

per unit length be greater than the modal loss per unit length:

$$n_g \frac{\gamma_A}{n_A} g_b - n_g \sum_i \frac{\gamma_i}{n_i} \alpha_i > 0. \tag{4.19}$$

We see immediately that the group index can be divided out of Eq. 4.19. This is because increasing n_g increases the time it takes light to propagate through the waveguide which increases both the gain *and* loss per unit length equally.

We see from the lasing threshold condition (Eq. 4.19) that increasing the group index will not help one reach the lasing threshold despite that fact that the gain per unit length increases. While above and below the lasing threshold the net modal gain depends on the confinement factor Γ, we see from Eq. 4.19 that the lasing threshold itself is determined only by the confinement of the electric field energy density (γ_A). Although γ_A is generally larger than the power confinement in the slot, it is always less than or equal to 1. Therefore the lowest lasing threshold for these structures is limited by the bulk material gain. An identical result can be derived by analyzing resonant cavities. In that case γ_A relates the material to modal gain per unit *time* [22].

Based on the threshold condition in Eq. 4.19 we can define a new figure of merit which represents how easily lasing can be achieved in a waveguide. Since in practice the modal loss α_m is often an experimentally measured parameter with units of inverse length, we can substitute this measured quantity into Eq. 4.19 and rewrite the lasing threshold condition as:

$$\gamma_b > \frac{\alpha_m}{\Gamma}. \tag{4.20}$$

This quantity α_m/Γ is a useful figure of merit since it is equal to the minimum bulk material gain needed to reach the lasing threshold in the waveguide. Because the group index cancels out in Eq. 4.18, this figure of merit can be di-

rectly compared for waveguides of different geometries to determine which can achieve lasing with the lowest material gain coefficient.

4.2.6 Scaling of Gain vs. Slot Thickness

While narrow slots enjoy greater local field enhancement, they also contain less gain material. Therefore the important question arises as to how the total gain in these structures depends on the slot thickness. As the width of the slot becomes increasingly narrow, the magnitude of the electric field increases until it reaches its maximum determined by the difference between dielectric constants in the high and low index region. This results in a greater stimulated (and spontaneous) emission rate of the material in the slot region [9]. According to the laser rate equations this should result in larger modal gain coefficients [23]. However, as the slot becomes increasingly narrow the area of the active region decreases. Therefore although the gain material is "working harder" there is less matter contributing to the gain. Thus it is important to understand how these competing phenomena affect the lasing threshold.

To minimize the lasing threshold we look for a maximum in the spatial confinement factor (γ_A) as a function of slot thickness which is plotted in Fig. 4.3(a). The maximum near a slot width of 60 nm illustrates the important point that the tradeoff between emission rate (which *increases* as the slot is narrowed) and material volume (which *decreases* as the slot is narrowed) results in an optimal slot width for minimizing the lasing threshold. Initially, as the slot narrows from 120 nm, the increased emission rate more than compensates for the decrease in volume of gain material, and γ_A increases. Near a thickness of about 50 nm

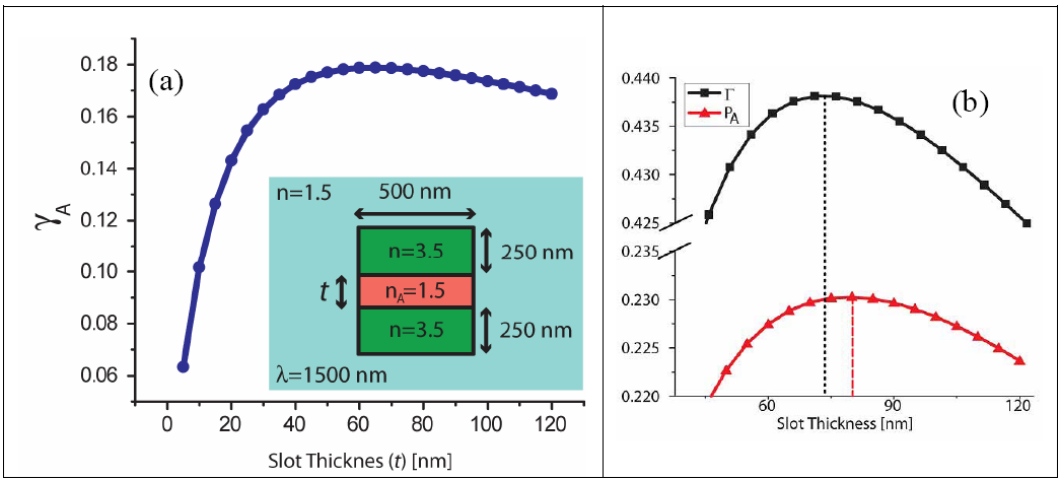

Figure 4.3: (a) The spatial confinement factor γ_A plotted as a function of slot thickness t, where the gain region is defined as the slot (pink region in inset) between the high-index rails (green). Narrow slots result greater emission rates of gain material while thicker slots provide more material which contributes to the gain. The peak in γ_A near a slot width of 60 nm indicates the condition where the combination of enhanced emission rate and volume of gain material result in the lowest lasing threshold. (b) The total confinement factor (Γ) (squares) and power in the slot region (P_A) (triangles) as a function of slot width. Dotted and dashed lines mark the slot widths which maximize Γ and P_A respectively. The discrepancy between these two plots shows that the percentage of power in the gain media is not an accurate indication of either the magnitude or the optimal design for modal gain.

the emission rate begins to saturate as it approaches its maximum value determined by the index contrast between the high and low index regions. After this point, further reduction of the slot thickness decreases the volume of material contributing to the gain without much enhancement of the emission rate, and the result is a sharp drop in γ_A.

As a comparison to previous methods, we plot in Fig. 4.3(b) the relative power confined in the slot region according to Eq. 4.17 and show again that slot waveguides outperform expectations based on previous theoretical treatments.

We see that *both* the magnitude of the modal gain *and* the optimal geometry are miscalculated using this method. The gain calculated numerically (in agreement with Γ) is nearly twice as large as would be expected based on the power confined to the slot mode. Additionally, the optimal slot width is miscalculated by more than 10% using power confinement.

4.2.7 Optimizing Slot Waveguide Geometry

To optimize the dimensions of a slot waveguide for an electrically pumped silicon laser, we apply the principles in the proceeding sections to achieve a waveguide design with a minimal lasing threshold. We estimate that the slot thickness should be no larger than 10 nm in order to achieve electrical injection via tunneling into an oxide-based gain media using bias voltages on the order of volts [6]. Therefore we keep the slot thickness fixed at 10 nm and compute the confinement factors as we vary the height and width of the waveguide. Here we have used the refractive indices of Si (3.48) and SiO_2 (1.46) as the high and low index material respectively, and a wavelength of 1.55 μm. We have assumed that gain only occurs in the slot region. Figure 4.4(b) - (d) show respectively the total confinement factor (Γ), the group index normalized to the slot index (n_g/n_A), and the energy density confinement factor (γ_A) as a function of height and width of the waveguide.

We see in Fig. 4.4(b) that the maximum modal gain for a 10 nm thick slot occurs near a waveguide width of 940 nm and a height of 340 nm (marked by the square) and has a value $\Gamma = 0.336$. Both the energy density and group index peak near a waveguide height of 340 nm. As the width of the waveguide

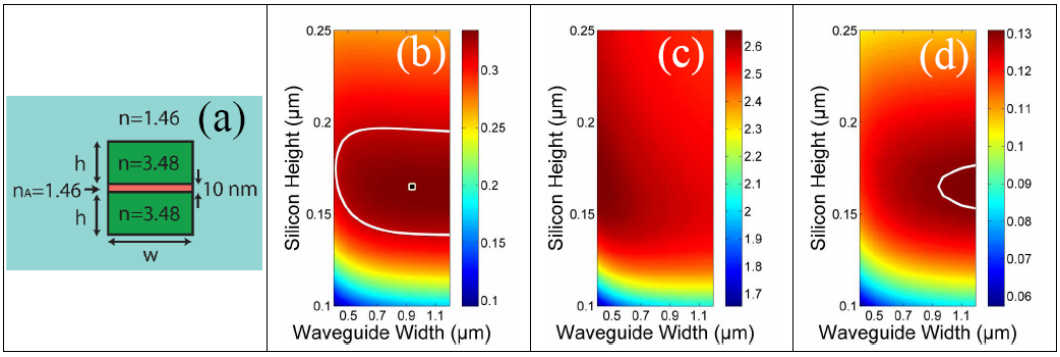

Figure 4.4: Optimization of width and height of $Si/SiO_2/Si$ slot waveguide with a 10 nm thick slot assumed to contain a gain medium. (a) Schematic of slot waveguide. (b) Total confinement factor Γ, proportional to the total modal gain. (c) Group index n_g divided by the slot index (1.46), which is responsible for the difference between the lasing threshold and modal gain. (d) Electric field energy confinement γ_A, inversely proportional to the lasing threshold. The maximum total modal gain is marked by the square in (a). The white contour shows the region which corresponds to a 5% change from the maximum values of Γ and γ_A.

is increased, the energy density in the slot region (and thus the net gain) increases. The group index, on the other hand, decreases with increasing waveguide width. These competing parameters result in a maximum Γ near a width of about 940 nm.

In contrast to the modal gain, with a fixed slot thickness, the minimal lasing threshold (determined by γ_A) shows no well-defined optimum. This is because the lasing threshold will scale only with the energy density confinement. The value of γ_A (Fig. 4.4(d)) increases monotonically with waveguide width and asymptotically approaches the value for an infinitely wide slab waveguide, which we calculate to have a maximum of $\gamma_A = 0.137$ for a waveguide height of 340 nm.

We see from Fig. 4.4 that the optimal device geometry is relatively insensitive

to variation in waveguide dimensions. Around the optimal design, variations of approximately ± 50 nm in the total height and width of the waveguide result in changes in the confinement factors of less than 5%. This allows the device performance to be relatively unaffected by size variations which can occur during fabrication.

4.2.8 Summary and Discussion

We have shown that some commonly applied metrics are not appropriate for determining gain in high-index-contrast waveguides, and from first principles developed several figures of merit to characterize waveguide structures for gain. In particular we have shown that the concept of power confinement to the gain region significantly miscalculates the gain experienced by the waveguide mode. Instead we have shown that the true confinement factor which determines gain per unit length results from the combination of group index and confinement of the electric field energy to the gain region. These terms can combine and in some cases exceed unity meaning that one can achieve greater gain per unit length than would be possible in the bulk material. The lasing threshold on the other hand only depends on the percentage of electric field energy in the gain region. To account for this we have introduced a new figure of merit to describe the suitability of a waveguide to achieve low-threshold lasing. This figure of merit is the experimentally measured propagation loss divided by the confinement factor introduced in this paper. The evaluation of this ratio determines the minimal material gain required to achieve lasing in the waveguide structure.

Additionally we have applied our analysis to the design of slot waveguide

structures. We have shown that the lasing threshold has a minimum for a particular slot width and increases dramatically as the slot is made thinner. Also we have shown that gain characteristics of the waveguides are fairly insensitive to variations in overall waveguide dimensions.

Since the confinement factors presented here were derived from perturbation theory, they can be applied to other phenomena in high-index-contrast waveguides including refractive index sensing. In deriving the confinement factors presented here we have studied gain as a perturbation of the imaginary part of the refractive index over a given region of the guided mode. The same formalism holds true for perturbations to the real part of the refractive index and therefore the confinement factors for gain presented in the paper can also be used as confinement factors for refractive index sensing [12, 21] and have shown good agreement with experiment [1].

In summary, this section provides the qualitative and quantitative analysis necessary in developing high-index-contrast waveguides with nanoscale light confinement for applications such as amplification and lasing.

4.3 On-Chip Gas Detection in Slotted Optical Resonators

4.3.1 Introduction

Interaction of light with matter in a gaseous state is an important functionality for sensors as well as for addressing isolated atomic or molecular states for quantum optic applications [24]. The vast majority of room-temperature exper-

iments involving light-matter interactions in integrated photonic devices have been performed with matter in the solid or liquid state [11, 25, 26, 27, 28, 29]. This is primarily due to the typically small refractive index and absorption differences between gasses at optical frequencies. Recently on-chip optical interaction with Rb vapor in ARROW waveguides was demonstrated by exploiting the enhanced optical interaction at atomic resonances [24]. In the absence of such atomic resonances, on-chip room-temperature optical interaction with gasses has remained unexplored, due to the relatively weak strength of interaction. In order to achieve on-chip optical interrogation of weakly interacting gasses we use a high confinement resonant cavity formed by slotted waveguides. Resonant cavities have proven to be extremely useful as sensors of change in refractive index [11, 25, 26, 27, 28, 29], and the slot waveguide geometry (as discussed in Chapter 2) allows us to enhance the light-matter interaction with the gas [11, 9, 12]. Therefore, by combining the enhanced light-matter interaction of the slot waveguide with the refractive index sensitivity of the microring resonator we demonstrate here the ability to detect small changes in the refractive index of surrounding gasses.

4.3.2 Experimental Setup

A scanning electron micrograph (SEM) of the 20 μm-diameter silicon microring like the one used for gas detection is shown in Fig. 4.5(a). The resonant wavelength of the devices is determined by the optical path length in the ring which depends on the effective index of the slot waveguide which, in turn, is determined by the refractive index of the gas surrounding the waveguide. Therefore by measuring changes in the resonant wavelength of the microring ($\Delta\lambda$) we

can detect small changes in refractive index of the gas (Δn_{gas})[11]. For changes in Δn_{gas} small compared to the core-cladding index difference, we can assume that the mode shape does not change. This is equivalent to taking the first-order correction to the resonant wavelength which can be expressed mathematically as:

$$\Delta\lambda = \lambda_0 \left(\Gamma / n_{eff}\right) \Delta n_{gas}, \tag{4.21}$$

where λ_0 is the unperturbed resonance wavelength, n_{eff} is the unperturbed value of the effective index in the ring, and Γ is the confinement factor as defined in Eq. 4.11 which satisfies the relationship $\Delta n_{eff} = \Gamma \Delta n_{gas}$.

Using a slot waveguide geometry we enhance the sensitivity of the resonance wavelength to changes in refractive index [12]. By virtue of the boundary conditions at dielectric interfaces, slot waveguides have been shown to greatly increase the electric field in the low-index slot region for the quasi-TE mode [4]. This has the effect of both increasing Γ according to Eq. 4.11 as well as lowering n_{eff} which increases the sensitivity to according to Eq. 4.21. Figure 4.5(b) shows a cross-sectional SEM of a slot waveguide like the one used in our device. Based on this geometry we use a finite difference mode solver to calculate the fundamental quasi-TE mode and plot the major electric field component in Fig. 4.5(c). The sidewall angles and waveguide dimensions of approximately 600 nm wide by 250 nm tall waveguide with a 40 nm slot (measured at the mid-point) are based on the cross sectional SEM in Fig. 4.5(b). From the results of the mode solver we calculate Γ and n_{eff} to be 0.64 and 2.01 respectively. Note that this large confinement factor means that the effective index of the slot waveguide changes by 0.64 times the change in index of the gas. This is a surprising result considering that only about 23% of the mode power resides in the gas region. This large confinement factor is the result of the enhanced electric field in the

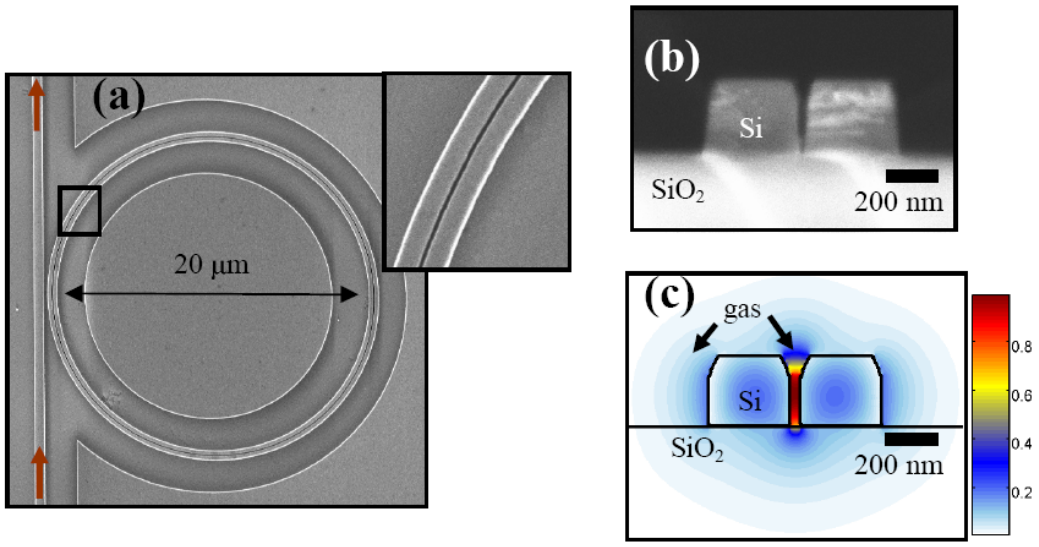

Figure 4.5: (a): SEM image of a silicon slotted microring resonator like the one used in our experiment. Inset shows the slot waveguide in the ring. Red arrows show direction of light propagation along the bus waveguide (b) cross sectional SEM image of a slot waveguide like the one in (a). (c) calculated mode profile for the major E-field component of the fundamental quasi-TE mode for the waveguide shown in (b). The high concentration of electric field in the gas region makes the resonator more sensitive to changes in refractive index of the gas.

region between the two silicon ridges as shown in Fig. 4.5(c). According to this ratio of Γ/n_{eff} we expect the slot waveguide to improve the sensitivity of the ring by a more than a factor of 20 compared to a waveguide with the same cross section without a slot. The sensitivity of the device is determined by the factor relating the shift in the resonant wavelength to the shift in refractive index $(\lambda_0\Gamma/n_{eff})$ which for our device is approximately 490 nm/refractive index unit (RIU). Due to the large index contrast and thus large interaction factor for our device, this quantity is more than a factor of two larger than previously reported slot-based resonant sensors for fluids [11].

To control the gaseous environment surrounding the ring resonator we affix

a 1 x 1.5 cm glass cell atop the silicon chip using a UV-curable epoxy. We attach flexible tubing connected to hose barbs on either end of the glass cell to control the type and pressure of the gas above the microring resonator. A photograph of the gas cell attached to a silicon chip is shown in Fig. 4.6(a). A schematic of the experimental setup is shown in Fig. 4.6(b). Our optical source is a fiber-coupled 5 mW tunable near-IR laser (1520-1620 nm) which is passed through an inline polarization controller (PC) which is adjusted to excite the quasi-TE mode. Using a cleaved fiber and an inverse nanotaper [30] we couple light into the waveguide at the chip edge. To distinguish guided from unguided light we offset the waveguide output by approximately one centimeter as depicted in Fig. 4.6(a) and (b). The light from the waveguide output at the chip edge is collimated with a collection less and passed through a polarization filter oriented to pass light polarized in the plane of the chip. The light which passes through the polarizer is measured with an InGaAs photodetector and power meter. By adjusting the PC to maximize the power through the polarization filter we can selectively excite and measure the quasi-TE mode. We record the transmission spectrum by scanning the wavelength of the tunable laser and plotting the collected power as a function of wavelength. Using needle valves we can control the flow of acetylene or compressed air over the chip. A pressure gauge at the output allows us to monitor the gas pressure in the system.

4.3.3 Measurement and Analysis

We determine the relative change in refractive index of gasses at various pressures by measuring changes in the resonant wavelength of the microring cavity. Figure 4.7(a) shows the transmission spectrum for the microring resonator in air

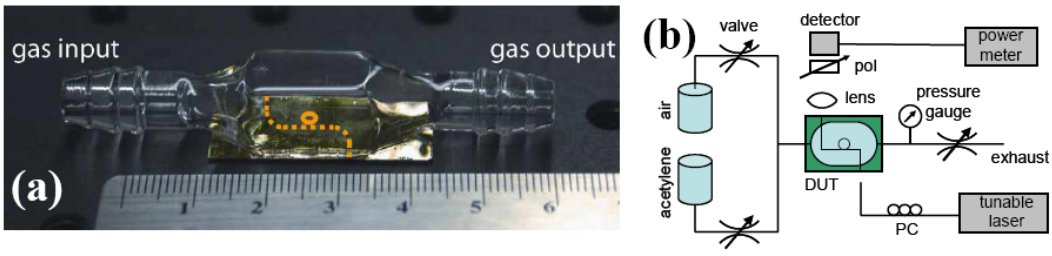

Figure 4.6: (a): Photograph of the gas cell affixed to the silicon photonic chip. Dotted line shows the path of the light through the waveguide and the circle denotes the approximate location of the microring. (b) schematic of the experimental setup which was used to measure the resonant wavelength of the microring under different gaseous environments.

(solid) and acetylene gas (dashed) at room temperature and atmospheric pressure. A resonance shift of approximately 0.2 nm is clearly visible. To confirm that the shift in resonance is due entirely to the difference in gasses we repeated the measurement 3 times alternating between air and acetylene. We calculate an average resonance shift of 0.19 nm with a standard deviation of 0.07 nm verifying that the shift in resonance is a reproducible consequence of the changing index of the surrounding gas. At room temperature and atmospheric pressure the difference in index between acetylene and air is approximately $3.24 * 10^{-4}$ RIU [31]. According to Eq. 4.21 this index difference should result in a resonance shift of 0.16 nm which agrees with the experimental data within one standard deviation. In Fig. 4.7(b) we plot the resonance wavelength as a function of acetylene gas pressure. For each pressure, we take three measurements over the course of approximately five minutes. We then fit the measured transmission data to a Lorentzian using a least squares method. Each symbol in Fig. 4.7(b) represents the average resonant wavelength from the three measurements as determined by the fit. The error bars represent plus and minus one standard deviation. Solid symbols represent the measured resonance shift as the cell is

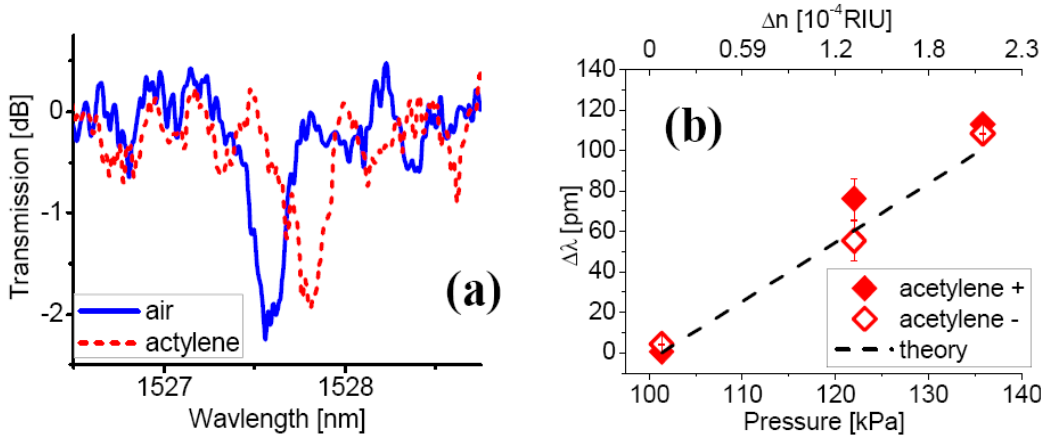

Figure 4.7: (a): Transmission spectra for the microring resonator in the presence of air (solid) and acetylene gas (dotted) at room temperature and atmospheric pressure. The shift in resonance is due to the difference in refractive index between air and acetylene gas. (b): Change in resonant wavelength as a function of gas pressure for acetylene. Solid and open shapes represent the average of three measurements for increasing and decreasing pressure respectively. Error bars represent the standard deviation of the three measurements for each data point. Dashed line shows the theoretical resonance shift based on the properties of the resonator. The slope of 490nm/RIU determines the sensitivity of the device.

pressurized and open symbols represent measurements as the cell is depressurized. The overlap of these measurements verifies that the shift in resonance wavelength is a reproducible result of the pressure of the surrounding acetylene gas.

We verify the measured index change due to variation in pressure by comparing it to the Gladstone-Dale model for the refractive index of gasses as a function of density. According to this model we can write the change in index of the gas (Δn) as a linear function of the change in pressure (ΔP):

$$\Delta n = \frac{K_{GD}}{RT} \Delta P, \tag{4.22}$$

where K_{GD} is the Gladstone-Dale constant, R is the ideal gas constant, and T is the temperature. According to [31] we compute the Gladstone-Dale constant for acetylene at a wavelength of 1527.5 nm to be $K_{GD} = 14.26$ cm^3/mol. Note that despite the weak molecular resonances which absorb in this wavelength range [32], to a good approximation K_{GD} can be considered to be constant. This is due to the fact that the overall refractive index of acetylene gas at 20 ^{o}C and atmospheric pressure is $n = 1 + 5.93 * 10^{-4}$ [31] which is due mostly to electronic transitions in the ultra-violet [33]. From the Kramers-Kronig relation we determine the maximum correction to the refractive index from the measured maximum absorption near 1527 nm (0.33 cm$^-1$) to be approximately $2 * 10^{-6}$ [34]. Since this correction is two orders of magnitude smaller than the background index we can neglect this effect and treat K_{GD} as a constant in this wavelength range. Using the room temperature of 20 ^{o}C and the calculated values of K_{GD} and Γ/n_{eff} we combine Eqs. 4.22 and 4.21 to plot the expected shift in resonance wavelength as the dashed line in Fig. 4.7. This theoretical resonance shift agrees with the measured data within the experimental error. To demonstrate the sensitivity of this device we can rewrite the x-axis in Fig. 4.7 in terms of the change in refractive index of the gas according to Eq. 4.22. This is plotted as the top x-axis in Fig. 4.7 showing that our device is sensitive to refractive index changes on the order of 10^{-4}. Note that the slope of the data in Fig. 4.7 is proportional to the ratio Γ/n_{eff}. Therefore the sensitivity of this measurement is proportional to the interaction factor and thus more than 20 times greater than the same device without a slot. One should note that the shift in resonant wavelength is dependent only on this ratio Γ/n_{eff} and independent of the cavity quality factor ($Q = \lambda_0/\Delta\lambda$, where $\Delta\lambda$ is the full width half maximum of the resonance). The ability to accurately quantify very small changes in the resonance wavelength

will be aided by an increase in Q since this results in a narrowing of the resonance linewidth ($\Delta\lambda$). Due to the large value of Γ/n_{eff} we were able to perform this experiment using a resonator with a relatively modest Q factor of about 5000. Much larger Q factors on the order of 10^6 and greater have been reported in similar structures by several groups [27, 35, 36] and could greatly improve this technique by allowing more accurate readout of the wavelength shift.

4.3.4 Summary

Using a silicon slotted microring resonant cavity we have demonstrated a chip-scale photonic system capable of detecting small changes in the refractive index of a gas due to composition and pressure. Due to the nanoscale slot geometry of our resonant cavity we have shown a large interaction factor of 0.64 indicating that the change in effective index of the slot waveguide is 64% of the change in index of the gas despite the fact that only 23% of the mode power resides in the gas region. This large interaction factor leads to a large device sensitivity of 490 nm/RIU. With this device we have demonstrated the detection of refractive index changes on the order of 10^{-4} using a resonator with a Q factor of 5000. Increasing this Q factor could further increase the accuracy of this detection scheme.

This platform for the interaction of gas-phase molecules with optical microcavities could open the door for a number of experiments in atomic and molecular optics as well as applications in gas sensing.

4.4 Summary

In this chapter we have presented two representative applications which benefit from confinement of light to nanoscale dimensions: silicon-based optical gain and gas sensing. We have developed confinement factors for describing how these devices perform and verified their accuracy numerically and experimentally. Based on our analysis we have shown that the enhanced light-matter interaction in these devices can greatly enhance their performance. In the case of optical gain we have shown that devices can operate more efficiently than one would expect based on the power confined to the gain media. In the case of sensing, we have used nanoscale light confinement in the slot waveguide to demonstrate the most sensitive optical-microcavity-based refractometric gas sensor reported to date.

BIBLIOGRAPHY

[1] J. T. Robinson, L. Chen, and M. Lipson, "On-chip gas detection in silicon optical microcavities," Opt. Express **16,** 4296–4301 (2008).

[2] J. T. Robinson, K. Preston, O. Painter, and M. Lipson, "Why Power Confinement Does Not Determine Gain in High-Index-Contrast Waveguides," Opt. Express (submitted).

[3] A. W. Fang, H. Park, O. Cohen, R. Jones, M. J. Paniccia, and J. E. Bowers, "Electrically pumped hybrid AlGaInAs-silicon evanescent laser," Opt. Express **14,** 9203–9210 (2006).

[4] V. R. Almeida, X. Qianfan, C. A. Barrios, and M. Lipson, "Guiding and confining light in void nanostructure," Optics Letters **29,** 1209–11 (2004).

[5] Q. Xu, V. R. Almeida, R. R. Panepucci, and M. Lipson, "Experimental demonstration of guiding and confining light in nanometer-size low-refractive-index material," Opt. Lett. **29,** 1626–8 (2004).

[6] C. A. Barrios and M. Lipson, "Electrically driven silicon resonant light emitting device based on slot-waveguide," Opt. Express **13,** 10092–10101 (2005).

[7] F. Ning-Ning, J. Michel, and L. C. Kimerling, "Optical field concentration in low-index waveguides," IEEE J. Quant. Elect. **42,** 885–890 (2006).

[8] H. G. Yoo, Y. Fu, D. Riley, J. H. Shin, and P. M. Fauchet, "Birefringence and optical power confinement in horizontal multi-slot waveguides made of Si and SiO2," Opt. Express **16,** 8623–8628 (2008).

[9] J. T. Robinson, C. Manolatou, L. Chen, and M. Lipson, "Ultrasmall Mode Volumes in Dielectric Optical Microcavities," Physical Review Letters **95,** 143901–4 (2005).

[10] *Confined Electrons and Photons*, E. Burstein and C. Weisbuch, eds., (Plenum Press, New York, NY, 1995).

[11] C. A. Barrios, K. B. Gylfason, B. Snchez, A. Griol, H. Sohlstrm, M. Holgado, and R. Casquel, "Slot-waveguide biochemical sensor," Opt. Lett. **32,** 3080–3082 (2007).

[12] F. Dell'Olio and V. M. Passaro, "Optical sensing by optimized silicon slot waveguides," Opt. Express **15,** 4977–4993 (2007).

[13] T. D. Visser, H. Blok, B. Demeulenaere, and D. Lenstra, "Confinement factors and gain in optical amplifiers," IEEE J. Quant. Elect. **33,** 1763–1766 (1997).

[14] H. Kogelnik, "Theory of Optical Waveguides," in *Guided-wave Optoelectronics*, T. Tamir, ed., (Springer Verlag, Berlin, 1990), pp. 7–87.

[15] L. A. Coldren and S. W. Corzine, *Diode Lasers and Photonic Integrated Circuits* (J. Wiley & Sons, New York, NY, 1995).

[16] C. Pollock and M. Lipson, *Integrated Photonics* (Kluwer Academic, Norwell, MA, 2003).

[17] J. Haes, B. Demeulenaere, R. Baets, D. Lenstra, T. Visser, and H. Blok, "Difference between TE and TM modal gain in amplifying waveguides: analysis and assessment of two perturbation approaches," Opt. and Quant. Electron. **29,** 263 (1997).

[18] J. D. Jackson, *Classical electrodynamics*, 3rd ed. (John Wiley & Sons, Inc., Hoboken, NJ, 1999).

[19] H. A. Haus, *Waves and fileds in optoelectronics* (Prentice-Hall, Englewood Cliffs, NJ, 1984).

[20] L. D. Landau and E. M. Lifshitz, *Electrodynamics of continuous media* (Pergamon Press, Reading, MA, 1960).

[21] G. J. Veldhuis, O. Parriaux, H. J. W. M. Hoekstra, and P. V. A. L. P. V. Lambeck, "Sensitivity enhancement in evanescent optical waveguide sensors," J. Lightwave Technol. **18,** 677–682 (2000).

[22] R. Perahia, O. Painter, V. Moreau, and R. Colombelli, "Design of quantum cascade lasers for intra-cavity sensing in the mid infrared," (submitted).

[23] A. E. Siegman, *Lasers* (University Science Books, Sausalito, CA, 1986).

[24] W. Yang, D. B. Conkey, B. Wu, D. Yin, A. R. Hawkins, and H. Schmidt, "Atomic spectroscopy on a chip," Nat Photon **1,** 331–335 (2007).

[25] L. De Stefano, L. Moretti, I. Rendina, and A. M. Rossi, "Porous silicon microcavities for optical hydrocarbons detection," Sensor Actuat A-Phys **104,** 179–182 (2003).

[26] B. Schmidt, V. Almeida, C. Manolatou, S. Preble, and M. Lipson, "Nanocavity in a silicon waveguide for ultrasensitive nanoparticle detection," Applied Physics Letters **85,** 4854–4856 (2004).

[27] A. M. Armani, R. P. Kulkarni, S. E. Fraser, R. C. Flagan, and K. J. Vahala, "Label-Free, Single-Molecule Detection with Optical Microcavities," Science **317,** 783–787 (2007).

[28] D. Englund, A. Faraon, I. Fushman, N. Stoltz, P. Petroff, and J. Vuckovic, "Controlling cavity reflectivity with a single quantum dot," Nature **450,** 857–861 (2007).

[29] T. Yoshie, A. Scherer, J. Hendrickson, G. Khitrova, H. M. Gibbs, G. Rupper, C. Ell, O. B. Shchekin, and D. G. Deppe, "Vacuum Rabi splitting with a single quantum dot in a photonic crystal nanocavity," Nature **432,** 200–203 (2004).

[30] V. R. Almeida, R. R. Panepucci, and M. Lipson, "Nanotaper for compact mode conversion," Optics Letters **28,** 1302–4 (2003).

[31] J. Gardiner, W. C., "Refractivity of combustion gases," Combust. Flame ; Vol/Issue: 40 pp. Pages: 213–219 (1981).

[32] K. Nakagawa, M. de Labachelerie, Y. Awaji, and M. Kourogi, "Accurate optical frequency atlas of the 1.5-μm bands of acetylene," J. Opt. Soc. Am. B **13,** 2708 (1996).

[33] P. Dub, L.-S. Ma, J. Ye, P. Jungner, and J. L. Hall, "Thermally induced self-locking of an optical cavity by overtone absorption in acetylene gas," J. Opt. Soc. Am. B **13,** 2041 (1996).

[34] R. W. Boyd, *Nonlinear Optics*, 2nd ed. (Academic, San Diego, CA, 2003).

[35] M. Borselli, T. Johnson, and O. Painter, "Beyond the Rayleigh scattering limit in high-Q silicon microdisks: theory and experiment," Opt. Express **13,** 1515 (2005).

[36] B.-S. Song, S. Noda, T. Asano, and Y. Akahane, "Ultra-high-Q photonic double-heterostructure nanocavity," Nat Mater **4,** 207–210 (2005).

CHAPTER 5

NOVEL PHYSICAL EFFECTS IN OPTICAL NANOSTRUCTURES

5.1 Introduction

In the previous chapters we have discussed the principals of nanoscale light confinement, performed measurements characterizing the optical modes, and demonstrated representative applications. In this chapter we focus on new physical phenomena resulting from nanoscale light confinement which could form the basis of future applications. Namely we show that an optical resonant cavity with a nanoscale mode volume can behave as an individual radiating dipole. We demonstrate for the first time that like a radiating dipole, the radiative lifetime of this cavity can be controlled by altering its physical environment even if these changes occur at distances which are large compared to the optical wavelength[1].

5.2 Far-field Control of Radiation from an Optical Nanocavity

Controlling the time that photons remain trapped in an individual state before being emitted is a fundamental challenge in photonics and quantum information processing. Optical resonant cavities allow one to trap photons for a period of time (photon lifetime) dictated by the cavity geometry. In active photonic devices such as switches, modulators, and buffers, it is often necessary to dynamically modify the photon lifetime (τ_p) of optical resonant cavities [2]. To

[1] Portions of this chapter are reproduced with permission from [1]

achieve this dynamic control of the photon lifetime several recent techniques have demonstrated tunable modification of τ_p. These current techniques including free carrier injection[3], thermal control [4], integrated fluidics [5], and near-field probes [6] all rely on physical changes within the near-field of the cavity (distances less than one wavelength).

In instances where physical modifications in the near-field are impractical, far-field control of the radiative properties can in principle be achieved by manipulating the local density of states at the source. It has been known for more than three decades that reflections at metallic or dielectric interfaces can modify the local density of states for optical dipoles resulting in a change of their radiative rate [7]. While far-field control of radiative lifetimes has been observed in atomic and molecular ensembles [8, 9, 10], only recently has this been achieved for individual optical dipoles using sensitive scanned probe experiments [11]. Here, applying similar techniques, we show the first far-field control of the radiative rate (or the photon lifetime) of an individual optical nanocavity and show it to be analogous to an individual radiating dipole.

5.2.1 Experimental Setup and Measurement

To demonstrate far-field tuning of the radiative rate of an optical nanocavity, we perturb the local density of states with a scanning metallic probe and extract the resulting change in radiative rate from the cavity's transmission properties. The effect of changing local density of states can be calculated by considering the interference between the source field and its reflection [12, 13]. An increase or decrease in the local density of states is equivalent to the reflected field con-

structively or destructively interfering with the source field. This results in an increase or decrease of the radiative rate depending on the phase relationship between the source field and radiation reflected by a metallic probe. By controlling the position of a scanning probe we tune this phase relationship between the source and reflected fields thereby controllably increasing or decreasing the radiative rate of the cavity. We increase the sensitivity of the experiment by working in a cavity configuration and extracting changes in radiative lifetime from changes in the cavity transmission. Using this technique we can detect lifetime modifications of less than one percent. This corresponds to a temporal sensitivity of less than one femtosecond for the cavity used in our experiment which has a photon lifetime of about 20 fs. This experiment enabled both by TraNSOM as discussed in Section 3.2 as well as the integrated resonant cavities with a nano-scale mode volumes described Section 2.3.

The optical nanocavity used in our experiment is embedded in a quasi-1D photonic crystal coupled to an input and output waveguide (as described in Section 2.3). The device is fabricated in silicon on insulator (SOI) using electron beam lithography and reactive ion etching. Fabrication details can be found in Section 3.2.4. As seen in the scanning electron micrograph (SEM) in the Fig. 5.1(a) inset, the nanocavity is defined by the two sets of holes separated by about 500 nm. These sets of holes act as quasi-1-D photonic crystals forming partial reflectors that trap light between them when the input wavelength matches the resonance condition [14]. The slot in the cavity center decreases the effective volume of the resonance cavity and increases the radiative rate as a result of the lower index contrast between the cavity and the cladding [15]. The experimental setup described in detail in Section 3.2.2 consists of amplified spontaneous emission filtered to $\lambda = 1565$ nm to match the cavity reso-

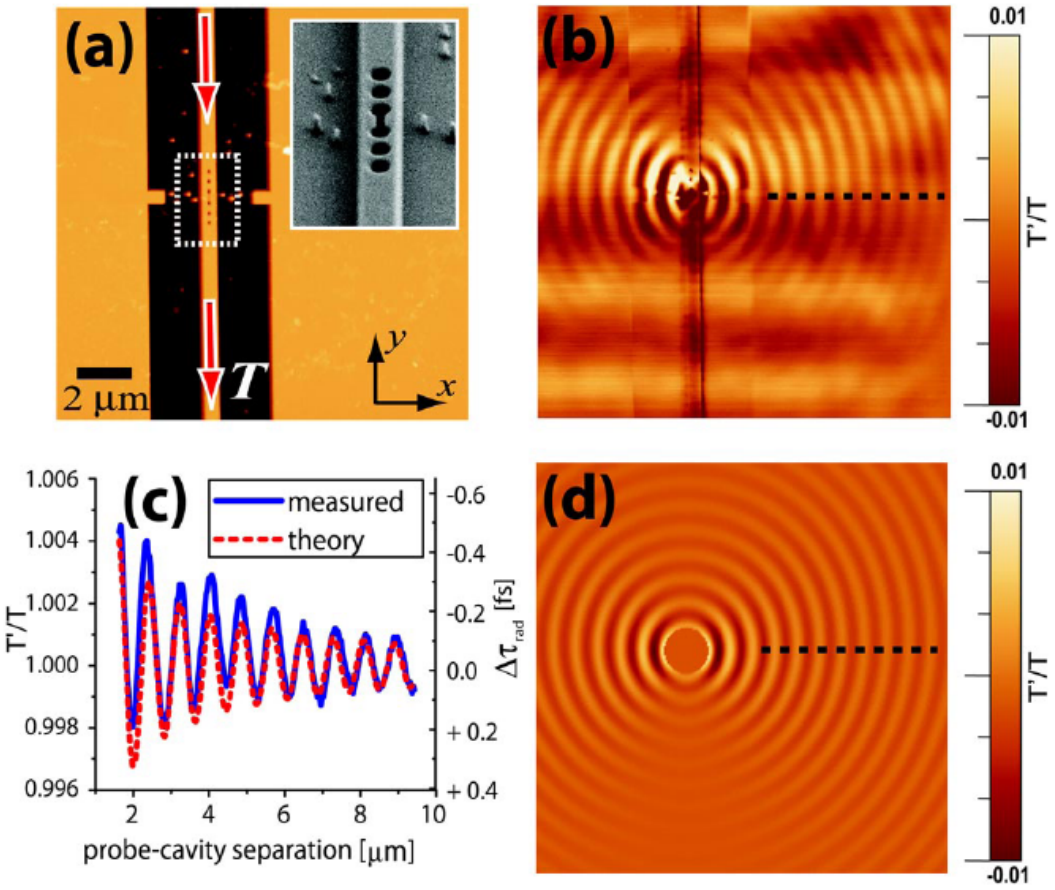

Figure 5.1: (a) Topography of the resonant cavity as measured by an atomic force microscope. Inset shows a scanning electron micrograph corresponding to the dashed box. Arrows show the direction of light propagation. (b) Measured transmission through the cavity recorded simultaneously with the topography in (a). (c) Measured (solid line) and calculated (dashed line) relative change in transmission (T'/T) and corresponding change in radiative lifetime ($\Delta\tau_{rad}$) as a function of the source-probe separation taken along the dashed line in (b) and (d) respectively. (d) Calculated change in transmission as a function of probe position based on the model in Fig. 5.2.

nance and coupled into and out of the device through optical fibers. The device is then imaged using a PtIr-coated probe in tapping-mode on an atomic force microscope (AFM) which simultaneously records the topography and power transmitted through the device. Note that the transmission is not demodulated at the tapping frequency. In tapping mode the amplitude of probe oscillation in the z-direction is about one hundredth of the optical wavelength used in this experiment. Therefore, the effect of probe oscillation on the change in radiative lifetime is negligible and the probe can be considered to be in contact with the surface. Figure 5.1(a) shows the topography of the resonant cavity as measured with the AFM and Fig. 5.1(b) shows the simultaneously measured change in transmission as a function of probe position. Figure 5.1(c) shows a cross section through the measured data and theoretical model taken along the dashed line in Fig. 5.1(b) and (d) respectively. Figure 5.1(d) represents a theoretical model for the experimentally measured change in transmission shown in Fig. 5.1(b). This model, based on probe-cavity interaction, is explained in detail in the following sections.

5.2.2 Theory and Analysis

To extract the change in τ_{rad} from the measured change in power transmitted through the cavity, we model the optical cavity as shown in Fig. 5.2(a). We can write the on-resonance cavity transmittivity (T) and reflectivity (R) of the cavity shown in Fig. 5.2(a) as [16]:

$$T = \left[(2/\tau_c)/(1/\tau_{rad} + 2/\tau_c)\right]^2, \tag{5.1}$$

$$R = \left[(1/\tau_{rad})/(1/\tau_{rad} + 2/\tau_c)\right]^2, \tag{5.2}$$

where τ_{rad} and τ_c are the radiative and coupling lifetimes respectively. Since absorption in small volume resonant cavities is negligible [17], τ_{rad} refers to the time it takes for the energy in the resonant cavity to decay by a factor of $1/e$ if the cavity is isolated from the input and output waveguides. Similarly to atomic dipoles, the stored energy is lost by radiation into free space which is determined by the local density of states. The coupling lifetime, on the other hand, refers to the time it takes light to couple into or out of the resonant cavity through the waveguides (Fig. 5.2(a)). It is important to note that unlike τ_{rad}, τ_c is independent of the local density of states and is determined only by the mode overlap between the guided mode in the resonator, the decaying Bloc mode in the 1D photonic crystal, and the waveguide mode [17]. Since the probe is several wavelengths away from the guided modes we can apply first order perturbation theory and assume that the mode profiles do not change as a result of the probe [18] and the overlap integrals which determine τ_c remain unchanged. The photon lifetime refers to the time it takes the energy in the coupled cavity (Fig. 5.2(a)) to decay by a factor of $1/e$ and can be written as: $1/\tau_p = 1/\tau_{rad} + 2/\tau_c$. Defining the ratio of the unperturbed radiative to coupling lifetimes as $\beta \equiv \tau_{rad}/\tau_c$, we can write the relative change in transmission in terms of the change in τ_{rad}:

$$\frac{T'}{T} = \left[\frac{\tau_p'}{\tau_p}\right]^2 = \left[\frac{1+2\beta}{\tau_{rad}/\tau_{rad}' + 2\beta}\right]^2. \tag{5.3}$$

Here the primes indicate the perturbed quantities. In principle β can be determined experimentally from the ratio of the on-resonance transmittivity (Eq. 5.1) and reflectivity (Eq. 5.2) of the resonator: $\beta = 1/2\sqrt{T/R}$ [16]. In practice this requires precise knowledge of the transmission and reflection coefficients at each optical fiber-to-chip interface. Since the positions of the optical fibers shift slightly during the adhesive curing process, the coefficients at these interfaces

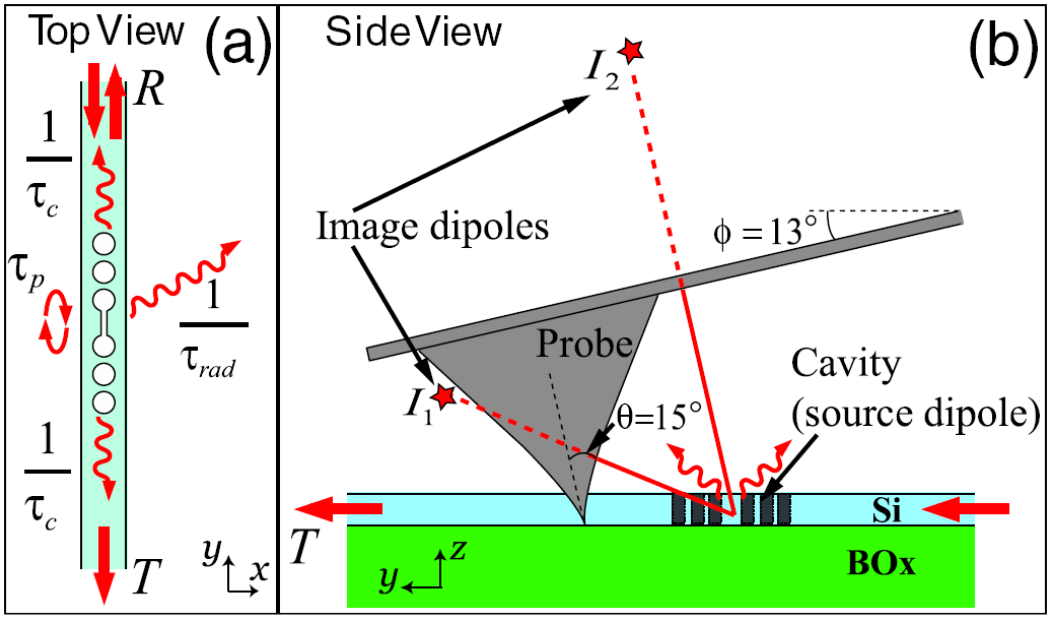

Figure 5.2: (a) Schematic of an optical resonant cavity coupled to the input and output waveguides where T and R are the transmittivity and reflectivity respectively (b) Model of the cavity-probe interaction as viewed from the side (not to scale). Stars labeled I_1 and I_2 represent image dipoles resulting from reflections at the probe apex and cantilever respectively.

vary significantly making the absolute transmission properties difficult to characterize. Instead we estimate β by simulating pulse propagation through the device using a 3D FDTD method. Using this technique we calculate an on-resonance transmittivity of $T = 0.48$ and reflectivity of $R = 0.10$ from which we estimate β to be 1.09. Note that we neglect the transmission change resulting from a shift in resonant frequency since for classical dipoles this effect is smaller than the change in τ_{rad} by a factor $1/\omega_0\tau_{rad} \ll 1$ [13]. Note that in Fig. 5.1(b) changes in τ_{rad} are observed at distances of more than nine microns from the source which corresponds to more than five optical wavelengths. This confirms we are indeed observing source-probe interaction beyond the near-field.

The oscillation of the transmitted power shown in Fig. 5.1(b-d) can be under-

stood by the model shown in Fig. 5.2(b) depicting a side-view of the cavity and the image dipoles resulting from the reflections by the probe. Reflection from the tip of the probe and the cantilever create two distinct image dipoles denoted as the stars labeled I_1 and I_2 respectively. As the probe position changes, the distances between the source and image dipoles change, altering the phase relationship between the source and reflected fields. Therefore, we expect τ_{rad} to oscillate as a function of probe position which we indeed measure in Fig. 5.1(b). Based on the geometry of the probe-cavity interaction in Fig. 5.2(b), we expect the lifetime oscillation due to I_1 to have a period of $\lambda/2\cos(\theta)$ where θ is the half angle of the probe cone near the apex as depicted in Fig. 5.2(b). Since θ is a small angle ($15 \pm 3^\circ$ according to SEM images of the probe) the period of the oscillation is close to half the free space wavelength (0.783 microns). This corresponds to the dipole-like radiation pattern centered at the cavity as shown in Fig. 5.1(b). On the other hand, lifetime oscillation due to I_2 should have a period of $\lambda/2\sin(\phi)$ where ϕ is the angle of the cantilever which is specified by the manufacturer to be $13 \pm 0.5^\circ$. This corresponds to a period of about seven microns and should vary only as the probe is scanned in the y direction. This is seen in as the long oscillations along the y direction measured in Fig. 5.1(b). Note that a scan along the y direction corresponds to a scan from right to left in Fig. 5.2(b) and a scan from bottom to top in Fig. 5.1(b). We verify the effect of both image dipoles by plotting in Fig. 5.3 the 2DFFT of Fig. 5.1(b). Indeed Fig. 5.3 shows distinct peaks at large wave numbers near $4\pi\cos(15^\circ)/\lambda$ (dotted circle) as well as peaks at small wave numbers along the y direction near $4\pi\sin(13^\circ)/\lambda$ (dashed lines). Note that the probe is modeled simply as a reflecting surface at an angle determined according to Fig. 5.2(b) and a reflectivity that contributes to the constant κ defined below. Probes of other materials or complex geometries with

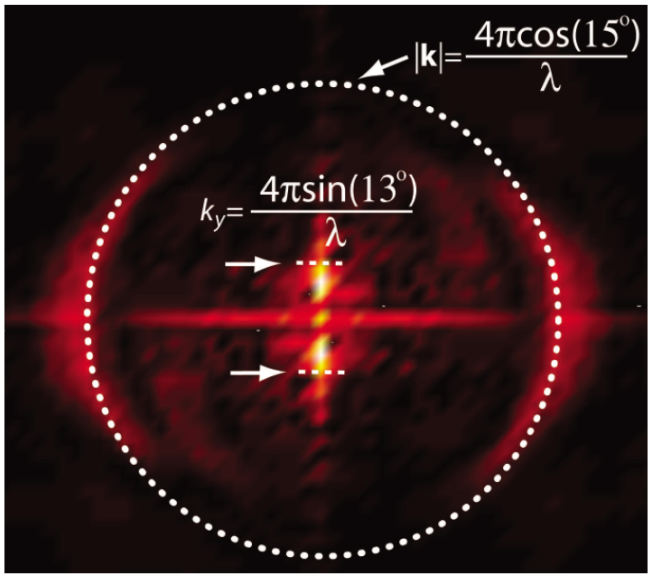

Figure 5.3: 2D FFT of the data in Fig. 5.1(b). Dotted circle shows the wave numbers corresponding to the probe cone half-angle of 15 degrees. Dashed line shows the wave numbers along the y-direction corresponding to the cantilever angle of 13 degrees.

multiple facets could allow for additional image dipoles of varying magnitudes which could result in a greater overall effect on the τ_{rad}.

To quantify the absolute change in τ_{rad} we mathematically express the above model and compare it to the measured data using a single fitting parameter. The field from the image dipoles interacts with the cavity (source dipole) perturbing its dipole moment. We write this perturbed dipole moment ($\mathbf{p}'$) as the sum of the unperturbed dipole moment ($\mathbf{p}$) and the effect of the image dipole: $\mathbf{p}' = \mathbf{p} - \kappa \mathbf{p} \mathbf{e}_p(\mathbf{r})$. Here the image dipole is represented as $|\mathbf{p}|\mathbf{e}_p(\mathbf{r})$ where $\mathbf{e}_p(\mathbf{r})$ is the electric field of a unit dipole at position $\mathbf{r}$ (determined by the probe position according to Fig. 5.2(b)) measured at the cavity position. This term is multiplied by the reflectivity of the probe and the effective polarizability of the cavity which we group as a single term κ which is our fitting parameter. Note from the minus sign proceeding $\mathbf{e}_p$ that we have assumed that reflection from the metallic

probe results in a π phase shift as expected from near-perfect metals. Since the radiated power is proportional to the square of the oscillating dipole moment [13] we can write:

$$\tau_{rad}/\tau'_{rad} = |\mathbf{p}'|^2/|\mathbf{p}|^2 = |\hat{\mathbf{p}} - \kappa \mathbf{e}_p(\mathbf{r})|^2. \tag{5.4}$$

We calculate the expected change in transmission as a function of probe position by first calculating the known radiation pattern of a unit dipole, combining Eq. 5.4 with Eq. 5.3, and taking the unit vector $\hat{\mathbf{p}}$ to be along the y direction (as suggested by Fig. 5.1(b)), and β to be the calculated value of 1.09. We then fit our model to the measured data using a least-squares fit along the dashed line in Fig. 5.1(b) with κ as the sole fitting parameter. According to the fit we determine $\kappa = 4\pi\varepsilon_0(6.3 \pm 0.1 * 10^{-22})\text{m}^3$ (which is about eight orders of magnitude larger than the polarizability of a single atom) and plot our model (dashed) and the measured data (solid) in Fig. 5.1(c). Note we have applied this fit over a region where the probe is more than one wavelength away from the cavity center. This is done to avoid probe-cavity interactions in the near field where the analogy between the nanocavity and a radiating dipole breaks down since one must consider the exact mode profile of the resonant cavity [19, 20]. The model shows excellent agreement with the measured data for large probe-cavity separations. For short separation distances, however, the measured data has a slightly longer oscillation period since the half-cone angle of the probe is smaller near the apex. We determine the unperturbed value of τ_{rad} from the full width half maximum (FWHM) of the resonance ($\Delta\lambda = 65 \pm 12$nm) and the calculated value of β according to $\tau_{rad} = (1 + 2\beta)\lambda_0^2/2\pi c\Delta\lambda = 63 \pm 13$fs. This can be derived from the definition of β and $\omega_0\tau_p \approx \lambda/\Delta\lambda$ [18]. Using the values of $\beta = 1.09$ and $\tau_{rad} = 63$ fs we calculate the absolute change in τ_{rad} according to Eq. 5.1 and represent those values as the y-axis on the right hand side of Fig. 5.1(c). Note

that by extracting the change in τ_{rad} from the change in transmission we are able to resolve changes of less than one femtosecond which would be extremely difficult to measure in the time domain. For high-Q cavities, however, such as those reported in [21] this long-range change in τ_{rad} could be on the order of picoseconds. Optimizing the probe geometry could also greatly enhance these long-range effects.

To verify that our model correctly predicts the measured transmission changes in two dimensions (Fig. 5.1(b)) we plot in Fig. 5.1(d) the simulated 2D probe-cavity interaction based on Eq. 5.1, the calculated value of β, and the fitted parameter κ. Note that in Fig. 5.1(d) we have only included the effect of the image dipole formed by the probe (I_1 in Fig. 5.2(b)) since this is the most sensitive to the probe position. We see that the simulated transmission changes in Fig. 5.1(d) indeed match the measured dipole-like pattern shown in Fig. 5.1(b). Note that Fig. 5.1(d) is generated based on the angle of *both* the probe *and* the cantilever as shown in Fig. 5.2(b). The small 13° angle of the cantilever causes the pattern above the cavity (positive y) to be slightly different than the pattern below the cavity (negative y). Although this effect is small, the fringes above the cavity are noticeably stronger than those below the cavity in both the measured (Fig. 5.1(b)) and calculated (Fig. 5.1(d)) images.

5.3 Summary

In this chapter we have discussed novel physical phenomena which occurs in nanoscale optical resonant cavities which could lead to future photonic applications. By controlling the position of a scanning probe in the optical far field we

have demonstrated the first far-field control of the radiative lifetime of an individual optical nanocavity. By extracting this change in τ_{rad} from the change in resonant cavity transmission we have demonstrated sub-femtosecond temporal sensitivity. Although the magnitude of change in τ_{rad} reported in this paper is less than one percent, these changes can be extremely precise and tunable. The magnitude can be increased by changing the reflectivity of the probe material or altering the geometry to allow for a greater number of image dipoles. The long-range control of radiative properties reported here could lead to advances in photonics, and quantum information processing, which require precise control over photon dynamics. We have also shown that radiation from photonic nanocavities is analogous to individual optical dipole radiation. This opens the door to new experiments controlling and characterizing the radiation properties of individual optical dipoles as well as photonic nanocavities.

BIBLIOGRAPHY

[1] J. T. Robinson and M. Lipson, "Far-Field Control of Radiation from an Individual Optical Nanocavity: Analogue to an Optical Dipole," Phys. Rev. Lett. **100,** 043902–4 (2008).

[2] M. Lipson, J. Lightwave Technol. **23,** 4222 (2005).

[3] V. R. Almeida, C. A. Barrios, R. R. Panepucci, and M. Lipson, Nature **431,** 1081 (2004).

[4] H. M. H. Chong and R. M. D. L. Rue, "Tuning of photonic crystal waveguide microcavity by thermooptic effect," IEEE Photon. Technol. Lett. **16,** 1528–1530 (June 2004).

[5] U. Levy, K. Campbell, A. Groisman, S. Mookherjea, and Y. Fainman, "On-chip microfluidic tuning of an optical microring resonator," App. Phys. Lett. **88,** 111107 (2006).

[6] I. Marki, M. Salt, and H. P. Herzig, "Tuning the resonance of a photonic crystal microcavity with an AFM probe," Opt. Express **14,** 2969 (2006).

[7] K. H. Drexhage, M. Fleck, H. Kuhn, F. P. Schafer, and W. Sperling, Ber. Bunsenges. Phys. Chem. **70,** 1179 (1966).

[8] E. Snoeks, A. Lagendijk, and A. Polman, "Measuring and Modifying the Spontaneous Emission Rate of Erbium near an Interface," Phys. Rev. Lett. **74,** 2459 (1995).

[9] R. M. Amos and W. L. Barnes, .

[10] J.-Y. Zhang, X.-Y. Wang, and M. Xiao, "Modification of spontaneous emission from CdSe/CdS quantum dots in the presence of a semiconductor interface," Opt. Lett. **27,** 1253 (2002).

[11] B. C. Buchler, T. Kalkbrenner, C. Hettich, and V. Sandoghdar, "Measuring the Quantum Efficiency of the Optical Emission of Single Radiating Dipoles Using a Scanning Mirror," Phys. Rev. Lett. **95,** 063003 (2005).

[12] R. R. Chance, A. Prock, and R. Silbey, "Lifetime of an emitting molecule near a partially reflecting surface," J. Chem. Phys. **60,** 2744 (1974).

[13] J. D. Jackson, *Classical electrodynamics*, 3rd ed. (J. Wiley & Sons, Inc, Hoboken, NJ, 1999).

[14] J. S. Foresi, P. R. Villeneuve, J. Ferrera, E. R. Thoen, G. Steinmeyer, S. Fan, J. D. Joannopoulos, L. C. Kimerling, H. I. Smith, and E. Ippen, "Photonic-bandgap microcavities in optical waveguides," Nature **390,** 143 (1997).

[15] V. R. Almeida, Q. Xu, C. A. Barrios, and M. Lipson, "Guiding and confining light in void nanostructure," Opt. Lett. **29,** 1209 (2004).

[16] H. A. Haus and Y. Lai, "Theory of cascaded quarter wave shifted distributed feedback resonators," IEEE J. of Quant. Electron **28,** 205 (1992).

[17] C. Sauvan, G. Lecamp, P. Lalanne, and J. Hugonin, "Modal-reflectivity enhancement by geometry tuning in Photonic Crystal microcavities," Opt. Express **13,** 245 (2005).

[18] L. A. Coldren and S. W. Corzine, *Diode lasers and photonic integrated circuits* (J. Wiley & Sons, Inc, New York, NY, 1995).

[19] A. F. Koenderink, M. Kafesaki, B. C. Buchler, and V. Sandoghdar, "Controlling the resonance of a photonic crystal microcavity by a near-field probe," Phys. Rev. Lett. **95,** 153904 (2005).

[20] W. C. L. Hopman, R. Stoffer, and R. M. d. Ridder, "Nano-mechanical tuning and imaging of a photonic crystal micro-cavity resonance," J. Lightwave Technol. **25,** 1811 (2007).

[21] B.-S. Song, S. Noda, T. Asano, and Y. Akahane, "Ultra-high-Q photonic double-heterostructure nanocavity," Nat. Mater. **4,** 207 (2005).

CHAPTER 6

CONCLUSIONS AND OUTLOOK

It is likely that over the next several decades photonics will play an increasingly important role in solving the looming problems in power consumption and footprint as communication and information processing demands increase. Implementation of photonic devices will likely occur everywhere from chip-to-chip and on-chip optical networking to components in network nodes in the telecommunications backbone. The future impact of these devices rely on (among other things) their efficiency. As discussed in this dissertation the efficiency of these devices is often related to the efficiency of the interaction between light and matter.

In this dissertation we have discussed the principles, measurement, and applications for enhanced interaction between light and matter via nanoscale light confinement. We have shown that in nanostructured dielectric materials it is possible to confine light to effective mode volumes much less than a cubic wavelength. To characterize these highly confined optical modes we have developed and implemented novel microscopy techniques which we have named TraNSOM and i-TraNSOM. Using the principles of nanoscale light confinement we have discussed how optical gain can be efficiently achieved on a silicon platform and demonstrated highly sensitive refractometric gas detection. Finally we have shown novel physical phenomena whereby nanoscale resonant cavities can be tuned with distant probes. We have shown that due to their small size these resonant cavities behave as individual radiating dipoles with radiative lifetimes which depend on their environment.

Throughout this text we have consistently found that due to the small length scales and large index contrast in semiconductor nanophotonics, many commonly held assumptions from the table-top and fiber optics community are not valid in this nanoscale regime. It is the hope of this author that in addition to the few technical advancements described in this dissertation the community can benefit from the knowledge that when working in this new regime it is important to investigate the subtleties of electrodynamics and continuously reevaluate concepts which are borrowed from other disciplines.